Near-Inertial and Tidal Currents detected with a Vessel Mounted Acoustic Doppler Current Profiler in the Western Mediterranean Sea

Elisa Garcia-Gorriz [1]* , Julio Candela [2] , Jordi Font [1]

[1] Institut de Ciencies del Mar (CSIC), Barcelona, Spain

[2] Centro de Investigacion Cientifica y Educacion Superior de Ensenada, Ensenada, Mexico.

* Present affiliation: Jet Propulsion Laboratory/California Institute of Technology, Pasadena, California, USA

Corresponding author address: Dr. E. Garcia-Gorriz, JPL/Caltech, MS 300-323, 4800 Oak Grove Drive, Pasadena, CA 91109. E-mail: eg@pacific.jpl.nasa.gov

Abstract. The Acoustic Doppler Current Profiler (ADCP) combined with accurate navigation provides absolute current velocities which include information from all the frequencies which have a dynamical presence in the ocean. The ADCP observations are, thus, intrinsically contaminated by signals which frequencies may not be useful for the scientific objectives of a given cruise. We propose a method that can successfully detect and separate the main high frequencies which are present in the ADCP measurements within a specific range. Our ADCP data sets were acquired during several cruises in the Alboran and Catalan sea (Western Mediterranean sea). Four current fields result from the method: tidal, near-inertial, steady and residual. We find that the resulting tidal semidiurnal, near-inertial and steady contain dynamical information and physical meaning: both the tidal and near-inertial fields fulfill the characteristics of observed and modeled fields in the Alboran and Catalan sea, while the time-independent steady component has high correlation with the geostrophic field. The residual field constitutes the portion of the ADCP observations which has no projection on the model considered and is, in fact, the misfit between the actual data and the model proposed.

near-inertial currents

tidal currents

1. INTRODUCTION

The Acoustic Doppler Current Profiler (ADCP) combined with accurate navigation (if no Bottom-Tracking mode is available during ADCP data acquisition) has revolutionized the way ocean currents are measured: the vessel-mounted version of this instrument provides a quasi-continuous vertical profile of horizontal current along the ship's trajectory [Candela et al., 1992; Kosro, 1985]. Once corrected for the ship's movement, these observations constitute the absolute velocity fields (referred to the terrestrial reference system) of the ocean current at a given time and 3-D location.

However, these velocity fields include information from all the frequencies which have dynamical presence in the ocean. Thus, the ADCP data are intrinsically contaminated by frequencies which may not be useful for the scientific objectives of an specific cruise. In general, the tides 'contaminate' the ADCP observations in this fashion and can mask subinertial currents. This situation is common in the world ocean with few exceptions. One of them is the Mediterranean sea, which has locally small tidal amplitudes (of a few cm). Nevertheless, the inertial frequencies (generated by wind events) can contribute significantly to the total current velocity field in some specific areas of the Mediterranean sea. This is the case of the Catalan sea (Fig. 1), where the subinertial circulation is weak.

In most of the world ocean, the presence of tidal variability in the ADCP data is unavoidable, especially in coastal regions where the tide can be the dominant signal present [Candela et al., 1992]. The inertial signal may not always be present in the data. When the focus of a dynamic study is the subinertial circulation, the tidal and inertial signals are the main candidates to contaminate the ADCP observations, thus requiring a method to reveal the wanted signal. The main difficulty involved in filtering tidal and/or inertial frequencies out of the observations is the double simultaneous variability (spatial and temporal) of the ADCP observations, which does not allow a simple harmonic analysis or lowpass filtering procedure as when dealing with time series of observations taken at a fixed location [Candela et al., 1992; Salat et al., 1992; Font et al., 1995].

To filter out the tidal signal from ADCP current velocities, three strategies have been used by the oceanographic community:

- The design of cruises which force ADCP acquisition to be repeated several times on the same ship tracks. Therefore, the tidal signal can be rebuilt applying harmonic analysis procedures [Lwiza and Bowers, 1990]. This strategy can be expensive and/or ship-time consuming.
- The use of tidal currents which are output of a numerical model and/or result from previous knowledge of the local tidal dynamics [Foreman and Freeland, 1991; Munchow et al., 1992].
- The use of techniques of empirical analysis to estimate the tidal currents directly from the ADCP measurements, but without repeating acquisition locations for the sake of the analysis [Candela et al., 1990a; Candela et al., 1992; Allen, 1995].

The last strategy is the antecedent of our study. It has been successfully applied to separate tidal currents in the Atlantic and the Pacific oceans. Our areas of study are the Alboran and the Catalan seas, both within the Western Mediterranean sea (Fig. 1). Our approach to the problem of filtering high frequency signals from ADCP measurements in these areas will focus in both near-inertial and tidal currents. Our method can separate the ADCP observations into four velocity fields, which are the tidal, near-inertial, steady and residual. The steady field is mathematically forced to be time-independent and will be compared with the geostrophic results from CTD observations, that were also performed during the studied cruises. The residual field constitutes the portion of the ADCP measured currents which has no projection on the model considered and is, in fact, the misfit between the actual data and the model proposed.

More specifically, the questions we examine are:

1- Is our method detecting the main high frequencies which are present in the ADCP measurements within a specific range? Which frequencies are these detected?

2- Have the resulting velocity fields (near-inertial, tidal, steady and residual) a physical meaning?

The paper is organized as follows: section 2 describes the temporal and spatial characteristics of the ADCP measurements as well as the method and ocean model considered in the present study. Section 3 shows the results which will permit us to discuss the two questions stated above in section 4. Section 5 has the conclusions.

2. DATA AND METHODOLOGY

2.1 Data description

The ADCP measurements analyzed in this paper were acquired in several cruises carried out in the Alboran and Catalan seas (Fig. 1).

In the Alboran sea:	In the Catalan sea:
FE92 (9/22 to 10/9/1992)	PR01 (5/15 to 5/22/1992)
OMEGA1 (9/30 to 10/4/1996)	PR02 (6/3 to 6/10/1992)
OMEGA2 (10/5 to 10/8/1996)	
OMEGA3 (10/8 to 10/11/1996)	

OMEGA1, 2 and 3 where performed sampling approximately on the same locations and few days apart from each other. In the same fashion, PR01 and PR02 were carried out in coincident locations in the Catalan sea and within an interval of few days. The FE92 cruise covered the entire Alboran sea and a section of it, from 9/22 to 9/27/92, is used in the detection of possible high frequencies present in the ADCP data.

The quality of the ADCP observations acquired during FE92, PR01 and PR02 was systematically controlled following the formulation described in Garcia-Gorriz et al. [1997]. Data with poor quality are dismissed for the present study.

The cruises FE92, PR01 and PR02 produced ADCP absolute velocity data corrected via Bottom-Tracking mode with nominal accuracy of 1 cm/s. For the ship transects with no Bottom-Tracking available, the ADCP absolute velocities were computed using the conventional GPS positioning system installed on the ship (R/V 'Garcia del Cid' for FE92, PR01 and PR02 cruises). The current profiles were recorded with a prescribed averaging time of 5 min and, thus, the accuracy of the GPS-corrected currents was 6.5 - 8.5 cm/s [Garcia-Gorriz et al., 1997]. To avoid the discrepancy of accuracies between Bottom-Tracking and GPS-corrected ADCP current observations, the current profiles have been averaged over one hour and the resulting accuracy is then 0.5 - 0.7 cm/s for the GPS-corrected profiles. Therefore, for the purpose of this study, we will assume that the resulting current fields have an accuracy of 1 cm/s.

Additionally, assuming that the ship had an average speed of 550 cm/s, the horizontal resolution of the velocity profiles is 20 km. This horizontal resolution is actually smaller because

the ship was not steaming continuously during the cruises. It stopped to cast the CTD stations. The ADCP acquisition was ongoing during these stops which typically lasted more than 0.5 h.

The cruises OMEGA1, 2 and 3 (onboard the R/V 'Hesperides') had 3-D and differential GPS available and the nominal accuracy value of the absolute ADCP current velocities was smaller than 1 cm/s.

2.2 Methodology

Model of ocean currents

The model of ocean currents that we assume is composed by two types of components: time-independent and time-dependent. Both of them are spatially (horizontally) variable. The range of signal periods that we consider in our study of the ADCP measurements is circumscribed to periods up to 1 day, which will theoretically capture near-inertial and tidal (semidiurnal and diurnal) signals in the ocean. These high frequency bands contribute significantly to the energy of the current velocity fields. A wider range of periods can be considered depending on the total time length of the ADCP records for an specific cruise.

The current velocity field is assumed to fulfill the following equation:

$$U(x, y, t) = U_{t\text{-}indep}(x, y) + U_{t\text{-}dep}(x, y, t) \qquad (1)$$

where U (x, y, t) are the eastward current component. An analogous equation to (1) can be written for the northward current component V(x, y, t).

For our range of signal periods, we split $U_{t\text{-}dep}(x, y, t)$ into a tidal and a near-inertial component of the velocity field. Equation (1) is then rewritten:

$$U(x, y, t) = U_{steady}(x, y) + U_{near\text{-}iner}(x, y, t) + \sum U_{tidal}(x, y, t) \qquad (2)$$

where:

$$U_{steady}(x, y) = F_{steady}(x, y) \qquad (3)$$

$$U_{near\text{-}iner}(x, y, t) = Fc_{near\text{-}iner}(x, y) * \cos \varphi(t) + Fs_{near\text{-}iner}(x, y) * \sin \varphi(t) \qquad (4)$$

$$\varphi(t) = 2*\pi* f_{near\text{-}iner}*t$$

$f_{near\text{-}iner}$: near-inertial frequency

$$U_{tidal}(x, y, t) = \sum [Fc_{tidal}(x, y) *\cos \phi(t) + Fc_{tidal}(x, y) *\sin \phi(t)] \qquad (5)$$

$$\phi(t) = 2*\pi*f_{tidal}*t$$

f_{tidal}: tidal frequencies

The variation of the steady field is restricted to the horizontal coordinates x, y. The time-dependent fields concentrate the time variation in the arguments of the sinusoidal functions. The respective amplitudes F(x,y) contain the spatial variation of the signal and their role can be described as horizontal interpolating functions. The number of tidal frequencies considered in the computation will depend on the tidal dynamics of the studied area. For our cruises, the detection of the main tidal frequencies contained in our ADCP measurements determines that the M2 is the most significant tidal component in both the Alboran and Catalan seas (see section 3.1).

The near-inertial amplitudes $Fc_{near\text{-}iner}(x, y)$ and $Fs_{near\text{-}iner}(x, y)$ could be multiplied by a decay or damping term e^{-ct}, where c is referred to as the e-folding time (normally with values between 4 and 12 days). This term arises from considering that the near-inertial currents are produced by sudden changes in the wind field. When the wind ceases, the induced oscillations slowly decay [Pollard and Millard, 1970].

We have initially attempted the near-inertial frequency detection considering the decay term e^{-ct} multiplying the amplitudes $Fc_{near\text{-}iner}(x, y)$ and $Fs_{near\text{-}iner}(x, y)$ in equation (4). A range of values from 2 to 15 days was tested for c. The near-inertial period detected from several tests shows no significant variation with respect to the case without decay, therefore we decided to dismissed the term e^{-ct} from equation (4) [Garcia-Gorriz, 1995].

The horizontal interpolating functions F(x, y) are arbitrarily chosen. Considering a purely tidal case, Candela et al. [1990a] concluded that the quality of the tidal fit was not very dependent on the choice of the functions. But they also concluded that a priori knowledge of the local tidal dynamics may help to find more appropriate specific functions. In the present paper, polynomials

are chosen to be the horizontal interpolating functions and are uniquely based in the ADCP measurements with no other dynamical assumption involved.

With independence of the set of horizontal interpolating functions which is used to compute (2), the system of equations to solve is:

$$\mathbf{A}\,\mathbf{c} = \mathbf{d} \qquad (6)$$

where **A** is the matrix containing the model (2) with dimensions (n, m): n is the number of available observations contained in vector **d** and m is the order of the model, which depends on the number of velocity field components used, i.e., steady, tidal or inertial, and on the degree of the polynomial chosen for each term. The order of the polynomial functions is prescribed and the parameters for each term are contained in the solution vector **c**. In this study we compute **c** in a least squares context using the singular value decomposition (SVD) of matrix A. In the case of an overdetermined system, SVD produces a solution that is the best approximation in the least squares sense; in the case of underdetermined system, it produces a solution whose values are smallest also in the least squares sense [Candela et al., 1992; Prunet et al., 1996].

Furthermore, the formulation permits weights associated with the ADCP observations to be introduced as additional input in the computation of (6). We performed several tests considering different sets of weights associated with the quality of the data sets. For example, the Percent-Good variable provided by the ADCP acquisition system for each profile. This relates to the percent of the acoustical signal echo received by the system during the acquisition interval: a low Percent-Good value does not guarantee that the associated echoes have enough energy to resolve the Doppler shift. During the quality control of the data, a threshold of 90% was imposed and out of range measurements were dismissed [Garcia-Gorriz et al., 1997]. However, the remaining observations still have their own Percent-Good assigned, as a measure of their quality. Apparently, the threshold we imposed during the data quality control was enough to assure the high quality of the remaining data because there was no significant variation of the results when the weights were introduced in (6).

In a first approach, we assume that the coefficients **c** in (6) characterize the kinematic pattern for the time and area of the cruise. Once a solution **c** is obtained a new **A** can be constructed for arbitrary points and times in the cruise area and then equation (6) will produce an interpolated - time and space- current field that fulfills equation (2).

For our choice of simple interpolating functions F(x, y), the degree of the polynomial functions in (3), (4) and (5) is prescribed. A hint to the adequate degree for $F_{steady}(x, y)$, for instance, comes from the previous knowledge that we have about the general circulation of an area: a priori, the degree for the western Alboran sea is expected to be higher (because of the presence of the anticyclonic gyre) than for the Catalan sea (with a relatively unstructured southwestward flow). However, the systematic criteria of the F-test was used to select the degrees of F(x, y). This test computes the quotient of the relative model variance and the relative misfit variance when increasing the degree of the polynomial functions. When the quotient is small, the model variance when increasing the degree does not improve compared to the misfit variance. With higher degrees and consecutive similar values of the quotient, the fit between observations and models improves, but the additional variance that will be explained will contain as much noise as information from the observations [Forsythe et al., 1977]. Hence, sequential F-tests with increasing polynomial degree values are performed and the choice is made at the step before the quotient drops below an unacceptable level (see section 3.2).

Detection of main frequencies from ADCP data

We make no a priori assumption about neither how many signals are contributing to the current velocity field nor what are the values of its corresponding frequencies. Therefore, we assume that the observations can be fitted by (1), with a time-independent plus a time-dependent field, and we iteratively vary the period in the argument of the latter to compute (6). The period iterations range from 11 to 25 h with a time-step of 0.1 h for each one of the cruise data sets. All our data sets are long enough to detect periods within this range. (Only in specific cases discussed below, the range is extended up to 130 h). The purpose of the iterations is to detect the signal periods that maximize

$$R = 1 - \sum [(u_{data}-u_{t\text{-}dep})^2 + (v_{data}-v_{t\text{-}dep})^2)] / \sum [u_{data}^2 + v_{data}^2], \qquad (7)$$

which represents the fraction of explained variance, and where u is the eastward and v is the northward component of the current velocity. To keep the consistency in the calculation of R, the field (u_{data}, v_{data}) is computed from $U(x, y) - U_{t\text{-}indep}(x, y)$ for each one of the iterations.

For this detection of signal periods, we only use the Bottom-Tracking corrected profiles with their acquisition time-averaging of 5 min. This was initially done to assure a large ADCP data set of profiles each 5 min and with a nominal accuracy of 1 cm/s. We tried to hold simultaneously the best possible accuracy and most frequent sampling available. We also repeated the detection with the complete data set (both Bottom-Tracking and GPS- corrected profiles) but 1h averaged to assure an accuracy of the latter within the interval 0.5 - 0.7 cm/s. The detected periods were coincident in both cases. To assure an accuracy of the order of 1 cm/s, and no larger, is important if we consider that the resulting time-dependent (near-inertial and tidal) fields will have values of about 10 cm/s or less (with the exception of the M2 tide in the western Alboran sea, with maximum values of 25- 30 cm/s).

3. RESULTS

3.1 Detection of frequencies from VM-ADCP data

For the Catalan sea cruises PR01 and PR02, the $U_{t\text{-}indep}(x, y)$ is subtracted from the $U(x, y)$ considering that $U_{t\text{-}indep}(x, y)$ can be fitted with a second-degree polynomial. The general circulation consists in a SW slope current of maximum values of the order of 50 cm/s [Font et al., 1988; Millot, 1987]. The resulting $U_{t\text{-}indep}(x, y)$ represents approximately 75% of the total current field. For the Alboran sea, a four-degree polynomial is fitted to the western anticyclonic gyre and represents about the 60% of the total current field. The results of the detection of frequencies shown in Fig. 2 and Table 1 are computed for the upper 60 m of the water column. Deeper, the main peaks that we observed remain for most of the available depths till 100 m.

The explained variance in equation (7) displays several bell- shaped hills, the maximum of which are interpreted as potential candidates to characterize an specific high frequency signal present in the ADCP data. The vertical scales of the 6 plots in Fig. 2 are not equal to enhance the visual effect of the peaks in the curve of R. However, PR01 and PR02 (Fig. 2 b, c) have a square in the point (12.4,0.2) and three stars are located (12.42, 0.35) for the OMEGA1, 2 and 3 plots (Fig. 2 d, e and f) to facilitate a visual reference of the differences between them. The solid vertical line in each plot labels the natural inertial period corresponding to the cruise mean latitude. The explained variance is plotted with the iterating period within the range 11 to 25 h.

Signals with periods within the interval 11 to 14 h:

The first value of the period we encounter that maximizes R is located at abscissa circa 12.4 h for the cruises FE92, PR01, OMEGA1 and OMEGA3 (Fig. 2a, b, d and f). For PR02 and OMEGA2 (Fig. 2 c and e), this peak is near 12 h (Table 1). This first peak for all of the cruises correspond to the M2 tide. Nevertheless, the M2 tide peak coexists with a higher peak of R for PR01 and OMEGA2 plots (Fig. 2 b and e), while for the rest of the plots is the highest. The maximum abscissa is 20.8 h for PR01 and 20.1 h for OMEGA2.

In the Alboran sea, the M2 tide for OMEGA1, 2 and 3 explains approximately the same amount of variance (see the reference star in Fig. 2 d, e and f). The amount for FE92 is 0.32. For OMEGA3 is 0.39. In the Catalan sea, the amount of explained variance by the M2 period is 0.17 for PR01 and 0.23 for PR02.

Signals with periods within the interval 14 to 18 h:

For all the cruises the peak found within this band is the third in importance, except for OMEGA1 and OMEGA3 where it is the second in importance. For OMEGA2, the peak at 16.3 h explains more variance that the one identified as the M2 tide.

Signals with periods in the interval 18 to 25 h:

With the exception of the ones for OMEGA1 and OMEGA3, all the rest of plots in Fig. 2 show a prominent peak within this period band which can be compared in importance to the one for the semidiurnal tide. However, it can vary in the amount of variance explained depending on the cruise: it explains slightly lower variance for FE92 and PR02, slightly higher for PR01 and distinctively higher for OMEGA2.

Other important feature of the peak (when existing) is its position with respect to the value of the natural inertial period (marked with a vertical solid line in Fig. 2 plots). For the Alboran sea cruises FE92 and OMEGA2, the period is smaller than the inertial one, although for the latter there is a difference of only 0.3 h. For OMEGA 1 and 3, the peaks correspond to much lower values of the variance explained. For the Catalan sea cruises PR01 and PR02, the peak has an abscissa which value is larger than the natural inertial period: 20.8 and 19.9 respectively. Except

for cruises OMEGA1 and OMEGA3, the abscissa value of the peak of R within this band will be interpreted as the near-inertial period (see Section 4.1).

Signals with periods larger than 25 h:

The western and eastern Alboran gyres were present during cruise FE92. We run the iterative procedure for the detection of frequencies in the ADCP data that covered the western Alboran gyre for a wider range of periods, from 25 to 130 h with 0.1 as time-step. The highest peaks in this band correspond to abscissa 30.8 h. There is also what can be interpreted as a extended sub-band that result from two lower peaks of R at 56 h and 105 h and which range approximately from 50 to 120 h. These should be related to mesoscale variability.

3.2 Resulting velocity fields

Consecutive F-tests where run to determine the degree of the interpolating polynomial functions F(x, y) in (3), (4) and (5). In each F-test run, the F(x, y) corresponding to one of the fields was varied, while the others were kept constant with a first guess value. Several tries with different first guesses where attempted to check the sensibility of the model (2). Additionally, each F-test run needed a near-inertial frequency prescribed. Thus, F-test runs were repeated considering values of the near-inertial period in the vicinity of the ones detected in section 3.1. The procedure was repeated for each one of the cruises. Fig. 3 illustrates typical F-test quotient results that we obtained. The figure corresponds to the PR02 cruise and shows the quotients for runs where the degree of the $F_{steady}(x, y)$ was increased from 0 to 8. The degree of the $F_{near\text{-}iner}(x, y)$ and $F_{tidal}(x, y)$ is 1 and kept constant. Fig. 3a, b and c show the same computation but considering three different near-inertial periods: 19.8, 20.0 and 20.2 h. The M2 tide period was used in these calculations. The abscissae of the plots in Fig. 3 display the sum of the degrees of the three F(x,y). The F-test quotients for the eastward and northward components were computed separately and when both had a simultaneous quotient drop that indicated which degree of the polynomial to use. Thus, the resulting degree for the steady field in PR02 cruise is 2 according to the F-test criteria. The results for the PR01 cruise are coincident with the ones for PR02. Therefore, for the Catalan sea the degree of the steady field in (3) is 2, and the near-inertial in (4)

and tidal in (5) are both 1. Likewise, from the F-test applied to the cruises in the Alboran sea, the degree of the steady field in (3) is 4 and the near-inertial in (4) and tidal in (5) are both 1.

3.2.1 Near-Inertial field

For FE92, PR01 and PR02, the upper (16m) and lower (more than 100 m) near-inertial currents are 180° out of phase. For PR02, it happens from 115 to 160 m. PR01 has similar results. Fig. 4a shows that a difference close to 180° is reached at 150 m and deeper for FE92. These results are consistent with what Salat et al. [1992] observed in the Catalan sea and Millot and Crepon [1981] in the Gulf of Lions. Likewise, they are consistent with numerical model results by Tintore et al. [1995].

As mentioned, once **c** is determined, a new **A** can be computed to calculate through equation (6) the near-inertial current field - in this case- at fixed points and times within the spatial/temporal domain of the cruise. The amplitude and phase of these currents were calculated for several points, considering a time interval larger than one inertial period. For each geographic point, the results represent the evolution of a single near-inertial oscillation. Fig. 4b plots the evolution of the phase and amplitude values which correspond to a location within PR02 domain. Each one of the polar plots displays consecutive times. This single near-inertial oscillation of approximately 10.4 cm/s is quasi-circular and clockwise. This clockwise evolution was common for the complete set of tested locations, though a few of them showed to be more elliptic than Fig. 4b. Analogous quasi-circular and clockwise plots are found for PR01 and FE92 (not shown).

A numerical experiment was performed to estimate the order of magnitude of the inertial currents. The model by Pollard and Millard [1970] was run with wind-stress forcing from ERS-1 winds for the time of the FE92 cruise. The equations to be solved are:

$$\left.\begin{aligned} \partial u/\partial t - f\,v &= F - C\,u \\ \partial v/\partial t - f\,u &= G - C\,v \end{aligned}\right\} \quad (8)$$

where f is the Coriolis parameter and also the natural inertial frequency, -c(u,v) is the decay or damping term, and F and G are the wind forcing terms given by:

$$(F, G) = \rho_a C_D U^2 (\sin\theta, \cos\theta) / (Z_0 \rho_w) \quad (9)$$

where ($U \sin\theta$, $U \cos\theta$) is the wind vector, C_D is the drag coefficient, ρ_a and ρ_w are the air and water densities respectively, and Z_0 is the depth of the mixed layer.

The model is run considering the location 4.5°W, 36.5°N in the northwest Alboran sea, which is coincident with a wind field grid point of the satellite wind data set and within the ADCP data domain. The ERS-1 wind data set we used had a horizontal resolution of 1°x 1° and we tried to force the model (8) with interpolated wind fields. The Z_0 is estimated to be 70 m from the CTD casts. The initial conditions for (u,v) in the system (8) are prescribed to be the concurrent near-inertial result, corresponding to the closest ADCP profile location and the model is set to be forced by the ERS-1 concurrent winds. Therefore, the initial time for the integration is also the concurrent time with the closest ADCP profile, which corresponds to the 9/24/92, one day after the last wind event. Initial inertial currents in the model equal to zero are not adequate, since inertial oscillations are likely to be already developed. The resulting currents from the model reach larger velocities than the amplitude of the near-inertial from ADCP. The u component is shown in Fig. 5. Three different decay coefficients are considered, 4, 8 and 20 days (Fig. 5 a, b and c). In the three cases, the wind forces the eastward component to reach values of about 17 cm/s, while our estimation from ADCP is approximately 10 cm/s for the location.

Different sets of initial conditions for u,v in (8) were tested to check the sensibility of the model. The integration of the model crashed if too large initial conditions were considered. The initial condition interval within which the model gave results was 10-25 cm/s. The corresponding maximum amplitude interval was 17-30 cm/s. Considering Z_0 = 100 m this interval is 12-19 cm/s.

3.2.2 Tidal field

For the Alboran sea, the resulting M2 ellipse orientations mainly exhibit zonally tidal motions. In general, these orientations are well correlated with the main orientation of axis of the basin and suggests the presence of the incoming Atlantic tide between 5.5 and 2°W (Fig. 6 for 16 m). In the northwestern Alboran basin the ellipse orientations are deflected towards the coast. The tidal current reaches about 25- 30 cm/s in the vicinity of the Strait of Gibraltar and decreases eastward progressively to values of few cm/s until longitude 2°W. For higher longitudes, the M2 tidal

motion is locally enhanced with values no larger than 10 cm/s and the ellipse orientations are approximately northeast between 2°W and 0°. The tidal currents for 156 and 250m (not shown) exhibit a similar pattern as in Fig. 6, with two main differences. The first one is that the amplitude decreases with larger depths, reaching a value of about 10 cm/s at 250 m near the Strait of Gibraltar, but also declining eastward. Secondly, the ellipse orientations at 156 and 250 m in the northwestern Alboran basin are more correlated with the isobaths than at 16 m and not deflected towards the coast. On the other hand, the ellipse orientations for tidal currents between 1°W and 0°are deflected towards the coast. The depth 250 m is the approximate depth of transition between the incoming Atlantic and outcoming Mediterranean water within the basin (this point is further discussed in section 4.2.3). For depths larger than 250 m, the resulting M2 tidal currents are of few cm/s even close to the Strait of Gibraltar.

For the Catalan sea cruises, the M2 component is the predominant tidal component though it does not dominate the background velocity field. The tidal currents are smaller than 5 cm/s at 16 m and the ellipse orientations are within the range 120- 180° in the area of study. The orientation of the major semiaxis of the ellipses suggest that the M2 tidal propagation is affected by the canyon shape of the topography (Canyon of Palamos) for PR01 and PR02 respectively. The amplitudes tend to be larger for PR02 than for PR01. The difference on average is of about 0.5 cm/s. This value lies within the accuracy range of the ADCP observations.

A numerical experiment is performed for cruises PR01 and PR02 to test both the robustness of the method and the potential physical description offered by our results. The hypothesis is that we can predict the M2 tidal signal at a given time once the coefficients **c** in (6), that characterize the kinematic pattern, are known. We have two sets of independently sampled ADCP observations (PR01 and PR02) on the same area of study and two corresponding sets of coefficients **c**. The day chosen for the prediction is June 6 at 0 hours. This date is out of the time frame of the PR01 cruise (15 days after the end of this cruise) and lies within the sampling time of PR02. Thus, the M2 tidal prediction is carried out from both PR01 and PR02. Fig 7 a and b display the resulting predicted M2 tidal ellipses for PR01 and PR02 respectively. These orientations are coherent with the local topography. Fig. 7 c and d show the contoured surface elevation tidal amplitudes, obtained by the fitted tidal transports and using the continuity equation,

as in Candela et al. [1992]. The difference between the predicted amplitudes is less than 1 cm/s and it lies within the accuracy range of the observations.

3.2.3 Steady field

The two quasi-permanent anticyclonic gyres which characterize the dynamical pattern circulation in the Alboran sea were fully developed during the FE92 cruise. The gyres are observed from the ADCP current velocities in Fig. 8a, and from the geostrophic field currents in Fig. 9a. Fig. 8b exhibits the fitted field which fulfills equation (2), taking into account both the M2 tidal and near-inertial frequencies detected. For the depth of 24 m, the correlation between the actual observations and the fitted field was 0.81 for the zonal component of the velocity and 0.78 for the meridional one. Up to 200 m, this correlations are higher than 0.7. As expected, the fitted field captures the two gyres. The residual field or mismatch between observations and our model in equation (2) does not catch the gyres and no obvious pattern can be detected (Fig. 8d). The steady field for 24 m is plotted in Fig. 8c. The correlation of this steady field with the geostrophic currents (Fig. 9a) is high: 0.78 for both components of the velocity.

The geostrophic velocities are calculated considering a reference level of zero velocity at 250 m. This depth has been selected after investigating the layer of minimum velocity from the ADCP observations, which provide a real-velocity scenario of the actual currents. Also, this layer of minimum velocity will be considered to coincide with the interface between Atlantic and Mediterranean water in the basin. However, the vertical transition between Atlantic and Mediterranean water is not abrupt but conditioned by local mixing, and the gyre-like pattern does not strictly allow to calculate a unique depth of no motion because of the accumulation of water (and bending of the isopicnals) due to the anticyclonic nature of the gyres. The interval of 250-300 m results to be the best candidate for the minimum velocity layer. The depth of 250 m is the approximate transition between the two waters.

The EOF analysis of the steady and geostrophic fields show that most of the energy of both fields is mainly concentrated in the first mode. Table 2 has the values for the first three modes. The first mode of the steady component has 69.27% of the energy, while the second has 18.69 and the third, 6.40. For the geostrophic field, the first mode accumulates 81.42% of the variability

and the second and third, 12.4 and 2.84 respectively. Both the vertical and horizontal patterns for the first four modes of the steady a geostrophic fields (not shown) are similar.

For the cruises in the Catalan sea, the correlation between the fitted fields and ADCP observations is 0.77 and 0.93 for the u and v current components during PR01 at 24 m. For PR02, they are 0.88 and 0.91 respectively. The ADCP observations for PR01 and PR02 are plotted in Fig. 10a and e; the respective fitted fields also in Fig. 10 b and f; the steady fields in c and g; and the residual in d and h. The main circulation in the area is characterized by a predominant SW flow. The geostrophic fields for the same depth captures it, as shown in Fig. 9 b and c, for PR01 and PR02 respectively. The eastern side of the SW flow exhibits the presence of dynamical structures which are interacting with this main flow. In comparison with the Alboran sea currents, the Catalan sea has smaller velocities associated with the SW flow. The depth of reference for the geostrophic calculations is 300 m, where the currents are very weak.

The similarity between the steady and geostrophic fields has been studied also with the help of the EOF analysis. Table 2 displays the percent of energy associated with the first three modes of PR01 for both fields. The values of PR02 are similar. The first mode accumulates significantly most of the energy in both the steady and the geostrophic cases, with notable analogy between them. The energetic first mode in both cases, captures the SW flow. On the other hand, the second mode of the geostrophic field shows a horizontal pattern which is locally correlated with the topography over the marine canyon, and also captures the interaction of other dynamical structures with the SW flow in the eastern side of the sampling area. The steady field retrieves none of these two situations in the second EOF mode. Those are present in the residual fields.

3.2.4 Residual field

This field contains the model misfit and therefore includes observational noise as well as all the other possible components of the observed field which have been dismissed. The non-steady mesoscale contributions will be included in this field, together with all the unaccounted frequency components of the current and other ageostrophic contributions. All of them have small magnitude in general, with locally enhanced values in certain areas. For FE92, PR01 and PR02 (Fig. 8d, 10d and 10h respectively), the aspect of the field does not exhibit an obvious structured pattern. Only for FE92, we can distinguish that small portions of the incoming Atlantic jet are

residing in this field, together with what can be interpreted as a small piece of the western Alboran gyre.

4. DISCUSSION

4.1 Detection of frequencies

Signals with periods within the range 11- 14 h: M2 tidal period

Once the time-independent signal has been removed from the data, what is left is fitted to a time-dependent signal of the form of (4) or (5). Those periods which are abscissae of peaks of the explained variance constitute the ones which have less misfit with the model of ocean currents assumed in (1), and, we infer that a signal with this period is contained in the ADCP currents.

In account of that, the M2 tide is distinctively detected in all of the cruises. The M2 tide is known to be the main tidal component in the Mediterranean sea [Candela et al., 1990a; Tsimplis et al., 1995; Alberola et al., 1995]. With the exception of the 11.9 h of OMEGA2, the rest of the periods lie within 0.2 h of the nominal value of the M2 period. Even when we have 11.9 h into account, the statistics of the M2 period for the six cruises still is 12.4 ± 0.3 h. Hence, we conclude that 0.3 h is a valid estimate of the accuracy of the periods detected following the methodology we presented in this study. Also, it is important to consider that with the limited (in time) amount of data from each cruise, we can not expect to extract a pure M2 component, but rather an estimate of the available semidiurnal energy in the observations. Using the M2 frequency to extract the semidiurnal variance present in the field works rather well though, since this is the principal semidiurnal component and also its frequency lies close to the center of the semidiurnal tidal band. Therefore, even though in various parts of the text we refer specifically to the M2 tide for convenience, we are actually referring to the mean semidiurnal patterns present in the observations.

In the Alboran sea, the variance explained by the M2 tide is within 0.32- 0.39, while it is within 0.17- 0.23 in the Catalan sea. We think that this discrepancy is explained by the larger values of the M2 amplitudes that the Alboran sea hosts, especially in the vicinity of the Strait of Gibraltar (Fig. 6). Therefore, a higher portion of the time-dependent signal is tidal. The R value for the three OMEGA cruises is very similar (see the reference star in Fig. 2 d, e and f) and higher

than for FE92. Likewise, PR02 displays a higher value than PR01. We have not an unequivocal explanation for these differences.

Signals with periods within the range 14- 18 h and 18- 25 h: Near- inertial period

OMEGA1 and OMEGA3 plots (Fig. 2 d and f) show no prominent peak in the 18-25 h band, unlike the rest of the cruises. It can be explained in the light of considering that the peaks within that band correspond to near-inertial currents and with additional concurrent wind field information. Fig. 11 displays the wind stress during each of the cruises. The sources of the wind data have been the ERS-1 and 2 and the NSCAT data sets. The available resolution of these satellite data sets (1°x1° for the ERS and 0.5°x0.5° the NSCAT data) allows an average of the wind stress in the area where ADCP were obtained and this information is indicative of the presence of wind events. Fig. 11a, b and c also show the standard deviation associated with the average of the wind stress.

For FE92, PR01, PR02 and OMEGA2 we see (Fig. 11a, b and c) that there were higher wind stresses close to the beginning of the cruises or less than 4 days before them, and they were followed by periods of relative calm. Thus, it can be concluded that the generation of wind-induced inertial currents was likely to occur and such currents had the opportunity to evolve and slowly decay with spatial coherence during the subsequent periods of calm. Inertial oscillations are considered to be predominantly locally generated and destroyed by surface winds and decay within 2 to 10 days [Pollard and Millard, 1970] and their near-inertial frequencies can be detected. In contrast, OMEGA1 and 3 have no clear distinctive presence of inertial oscillations. OMEGA1 data were acquired during continuous wind events and it is conceivable that inertial oscillations were consecutively excited and extinguished by the surface wind in such situation. On the other hand, OMEGA3 data were obtained after an extended period of lack of wind events and, thus, no generation of inertial currents.

The peaks in the band 14- 18 h have no definite identification. The value of the variance explained is lower than that corresponding for the near-inertial and tidal peaks. Only in the case of OMEGA2 (Fig.2 e), this peak has a slightly higher R than the tidal one. One could discuss that the peaks in the band 14-18 h are also potential candidates for the near-inertial period (if we momentarily forget about OMEGA1 and OMEGA3). However, their low values of R compared

to tidal and near-inertial prevents us from it. And, furthermore, the near-inertial periods that we find are consistent with previous studies in the area. The cases of PR01 and PR02 are clear examples [Salat et al., 1992].

The near-inertial periods are smaller (or almost equal) than the natural inertial one for the Alboran sea cruises, which is a common situation when near-inertial oscillations are observed in the ocean. The near-inertial frequency is generally within a range of 3% to 20% higher than the local inertial one f. Wind activity generate oscillations with frequency ω within $f \leq \omega \leq N$, where N is the Brunt- Vaisala frequency. For FE92, the near-inertial frequency is 19.1 h, and for OMEGA2 it is 20.1 h, while the natural inertial period is 21.3 h. In contrast, for the Catalan sea the near-inertial periods are larger than the inertial one, which is 18 h. They are 20.8 for PR01 and 19.9 h for PR02. All these results for both the Alboran and the Catalan sea are affected by an error bar of at least ± 0.3 h. The detected near-inertial periods in the Catalan sea are consistent with results by other authors in the area and this phenomenon is due to the fact that the near-inertial oscillation is nested in a region of anticyclonic vorticity [Salat et al., 1992]. In fact, they analyzed currentmeter and drifter measurements in an area located 80 km downstream of the location of PR01 and PR02. Likewise, Font et al. [1990, 1995] concluded that the SW flow fluctuations which are mainly detectable in spring and summer (which is the time frame of PR01 and PR02 cruises)- during the stratification of the water column - correspond to near-inertial oscillations.

Finally, there are three more related issues to discuss in relation to the reliability of the technique to detect frequencies from ADCP data. In the first place, we checked if the technique would add some noise (maybe in the form of peaks of R) due to the spatial and temporal sampling of the ADCP measurements. We repeated the frequency detection for all of the cruises replacing the actual currents with random values which had the same average order of magnitude as the measurements. The actual temporal and spatial coordinates were kept the same. The results showed a random pattern for all of the cruises. We conclude that no spurious frequency is added by the method. Fig. 12a shows this result for FE92 as a representative example.

Secondly, we checked the reliability of the detection procedure replacing the actual data of the cruises by a pure M2 tide signal generated in the actual time and spatial locations. In this case the

method detected the M2 tide optimally, with R=1 as expected for period 12.42 h for all the cruises. Fig. 12b displays the results for OMEGA1 as an example.

To conclude, the complex demodulation technique was applied to the cruise data sets. It is an alternative way to detect the frequencies based on the formulation of Hebert and Moum [1994]. The main difference with our methodology is that we assume and allow spatial variability of the signal through the interpolating functions F(x, y) while their formulation ignores it. Our technique integrates both time and space information in the detection of frequencies and computation of the resulting time-dependent current fields. In addition, a positive secondary result of the complex demodulation calculation performed here is that we will verify the implicit assumption of existence of spatial coherence for the signals. The resulting frequencies detected by complex demodulation were significantly coincident, but the relative importance of the peaks (near- inertial higher than tidal or reverse) varied in some few cases with respect of our results in Fig. 2. Fig. 12c and d displays the two discrepancies we got. For PR01, the M2 tide is clearly detected, and also the 16.5 h peak, but the near-inertial period is 20.2 in stead of our 20.8 ± 0.3 h. In addition, the tidal peak is higher than the near-inertial one in complex demodulation, while in our case it was the reverse. For OMEGA2, the height of the peaks is also reversed and the M2 tidal period is located in 12.4 h here, while our method gave 11.9 ± 0.3 h. The other two peaks are the same for both methods. What we conclude from these results is that our estimate of the error bar of the detected frequencies is possibly larger than 0.3 h for our technique and ± 0.6 h would be more appropriate.

Signals with periods larger than 25 h:

We have not identified the detected signal corresponding to the period of 30.8 h (Fig. 13). However, considering that for the western Alboran gyre the maximum radius is within 50-70 km and the ADCP recorded currents in these locations are about 90- 110 cm/s, the resulting range of periods that correspond to a circular movement is 95- 110 h. This periods lie within the band 50-120 h observed in Fig. 13. Furthermore, the Alboran gyre forms a system of nested gyres with decreasing radii and current velocities. The range of periods of these nested circular movements are likely to appear in the mentioned band plotted in Fig. 13.

4.2 Resulting velocity fields

4.2.1 Near-Inertial field

One could argue that Fig. 4b plots can be interpreted as an extrapolated near-inertial evolution, since on this particular location only one ADCP observation was registered, and only one near-inertial current vector is filtered out from it. However, the results displayed in Fig. 4b are to be interpreted as an approximation of the evolution of a single near-inertial wave if the basin currents fulfilled equation (2) and these currents were well described with the coefficients **c** in equation (6) within the spatial/temporal cruise domain. Thus, the difference of phase of 180° between the upper and lower currents, the clockwise direction of rotation and the almost-circular shape indicate that the field is likely to be considered of the near-inertial type.

The results of applying the model of Pollard and Millard [1970] to estimate the order of magnitude of the wind-induced currents in the Alboran sea show that the depth of the mixed layer Z_0 conditions the maximum value of the currents. Initially, we considered Z_0 = 70 m. The criteria to chose the depth of the mixed layer are diverse. The one we initially used was considering the depth at which the gradient of temperatures was maximum. The location is out of the gyres and, thus, the vertical contrast of salinities is less pronounced than the thermal one. However, considering Z_0 = 100 m, the values from the model are much closer to our estimation of the near-inertial vector, if the initial condition is set to be 10 cm/s. There are few specific studies about the near-inertial oscillations in the Alboran sea. Viudez [1994] detected these oscillations through the analysis of currentmeter observations. The maximum near-inertial velocities were about 30 cm/s close to the surface and 5-10 cm/s at depths down to 600 m. In conclusion, the model gives slightly higher values for the wind-induced current than our estimations, but not in total disagreement: 17 cm/s if Z_0 = 70 m, and 12 cm/ s if Z_0 = 100 m, considering 10 cm/s as initial condition of the model.

In the Catalan sea, it has been observed that the near-inertial currents can significantly contribute to the absolute current velocity field [Salat et al., 1992]. Our estimates from ADCP are, as in the case of the Alboran sea, lower than what has been observed by currentmeters.

4.2.2 Tidal field

The tides in the Mediterranean sea result from the interaction of direct tidal forcing within the sea and the co-oscillating tide coming in from the North Atlantic through the Strait of Gibraltar [Candela et al., 1990b]. The propagation and significance of the tide through the Strait of Gibraltar into the Alboran sea has long been a point of disagreement [Thomson et al., 1998]. Observations show that the North Atlantic tidal ranges are in excess of 2 m while the Western Mediterranean are less than 1 m [Candela et al., 1990b]. This incoming wave from the Strait of Gibraltar is important in tuning the tides in the whole of the Mediterranean sea: the tides up to approximately 1 °E are mainly determined by the incoming Atlantic wave; farther east their effect is important for modifying the response to the equilibrium tide [Tsimplis et al., 1995]. Our results in Fig. 6 show that the larger values of the M2 tide in the Alboran sea are reached in the vicinity of the Strait of Gibraltar, with 25 cm/s and decreasing eastward within the basin. The M2 ellipse zonal orientation suggests that the resulting M2 tide contains a significant contribution of the incoming Atlantic tide through the Strait. Farther east, the M2 tidal motion reaches values of few cm/s and the ellipse orientation also follows approximately the orientation of the axis of the basin. Our results are consistent both qualitative and quantitatively with observations [Alberola et al., 1995] and numerical models results [Lozano and Candela, 1994; Tsimplis et al., 1995]. The M2 ellipse orientation from the model by Tsimplis et al. [1995] displayed a basin-axis orientation: zonally between 5.5 and 2 °W and approximately northeast between the latter and 0 °. Their amplitudes were also consistent with our results, with maximum values of 20 cm/s from the model in the vicinity of the Strait of Gibraltar and decaying eastward. Alberola et al. [1995] observed that the tidal currents can reach the maximum values of 60 cm/s at depths within the range of 200-300 m in the east side of the Strait. At the surface, they also observed maximum tidal currents of 100 cm/s.

There are two possible sources for the semidiurnal tidal motions in the ocean: barotropic currents associated with the basin-scale barotropic (surface) tide and baroclinic currents generated by the barotropic tide in stratified regions with steep topography [Thomson et al., 1998]. Tsimplis et al. [1995] concluded from tidal model experiments that the baroclinic tidal component might be of secondary importance in the area, with small surface amplitudes. Candela et al. [1990b] also pointed out that the structure of these M2 tidal currents is principally barotropic, and the interface

between Atlantic and Mediterranean waters masses exhibits vertical excursions at the tidal periods, especially within the Strait. From our resulting tidal fields at different depths, the barotropic character is approximately fulfilled down to 200 m in the basin, especially close to the Strait of Gibraltar. It is not fulfilled in the northwestern area of the basin and for locations between 1 °W and 0 °.

In the Catalan sea, the M2 tide is also detected. The amplitudes of the tidal currents are small, less than 5 cm/s for both PR01 and PR02 and the orientation of the major semiaxis is coherent with the local topography. The results of the numerical experiment helps us to conclude that this formulation is robust enough not only to filter out the tidal signal, but also to allow a consistent tidal prediction of the horizontal fields from two sets of independently sampled ADCP observations in the same area. The difference in the prediction lies within the range of the accuracy of the ADCP observations.

We conclude that the resulting tidal signal has a physical meaning for both Alboran and Catalan seas.

4.2.3 Steady field

The Alboran sea is the first Mediterranean basin encountered by the incoming Atlantic water through the Strait of Gibraltar - with salinities smaller than 36.5- and the last basin occupied by the outflowing Mediterranean water - with salinities larger than 38.4 [Kinder and Parrilla, 1987]. These two waters exhibit maximum contrast in the Strait and they coexist and continue to mix in the Alboran basin. The mixing generates the so-called Modified Atlantic Water (MAW), with a salinity range between 36.5 and 37.5. The dynamics in the Alboran sea is mainly conditioned by this contrast of density, topography and winds. The horizontal pattern of circulation is characterized by the presence of two quasi-permanent anticyclonic gyres located respectively in the western and eastern part of the Alboran basin [Heburn and LaViolette, 1990], and as seen in Fig. 8a and 9a.

In the Alboran sea, the steady and the geostropic fields have very high correlations and the vertical and horizontal patterns of the firsts EOF modes are similar. We conclude that the steady field captures the main dynamical characteristics offered by a geostrophic study in the basin. In the case of the Alboran sea, the dynamical pattern is dominated by the two anticyclonic gyres, with

small contribution from the tidal and near-inertial fields. Only in the close vicinity of the Strait of Gibraltar the tidal current can be significant with respect to the background field.

The steady field is mathematically time-independent in the present formulation. However, as seen in the steady fields resulting from PR01 and PR02, this field varies in an interval of 10 days. This variation is reflected in small changes of position of the predominant SW flow on the slope, probably due to the interaction of the flow with dynamical structures in the east side of the sampling area (Fig. 10 c and g). The change is more evident when observing the geostrophic fields (Fig. 9 b and c) which seem to be bent by the downstream canyon topography during PR02 and also exhibits the presence of meandering structures in the east side. From the EOF analysis, we conclude that the steady field captures well the very energetic first mode. However, it is not able to catch the interactions of the flow with topography or lateral meandering structures, which we believe can be considered as a mesoscale structure. Concurrent sea surface temperature were examined and these formations were not permanent, with diverse horizontal distributions. Font et al. [1988] observed analogous patterns and pointed out the mechanisms that can trigger the formation of meandering structures close to the SW flow.

Even if our strictly time-independent steady field cannot be fully identified with the geostrophic field, we believe that the comparison between them helps us to verify the physical meaning of this component and to understand better its dynamic content. Fig. 14 a and b show the difference between the geostrophic velocity and the steady field for PR01 and PR02 respectively. These plots illustrate, but do not quantify, phenomena and allow us to better discuss the physical meaning of the steady field. Over the submarine canyon, PR01 and PR02 show different tendencies, which we attribute to the topographic effect on the SW flow when this is located in two different positions. This conclusion is consistent with what Font et al. [1993] found from observations (drifters) for the same cruises. One of the drifters deployed during PR01 followed approximately a trajectory as if it was carried by the residual currents in Fig 14a: it entered the canyon, was briefly deflected to the northeast to later exit the canyon following the topography. First, a SE shift of direction followed by a SW. For PR02, there is a recirculation structure in the southern part of the canyon.

4.2.4 Residual field

The portions of the incoming Atlantic jet and the western Alboran gyre that remain in the residual field for FE92 correspond to a small fraction of the energy carried by such structures. The relative flexibility of the polynomials that we used could be one of the reasons for that, together with the non-accounted signals considered in equation (2).

The Fig. 15 a, b and c plots the sum of the steady and residual field for FE92, PR01 and PR02 respectively. These fields correspond to the currents velocities having only filtered the M2 tides and the near-inertial components out, but with all the remaining dynamical information of the fields. This was the main objective when we initiated the present study: to filter out high frequency components in vessel mounted ADCP data, in order to obtain better velocity fields for mesoscale dynamic studies.

5. CONCLUSIONS

We conclude that our method is successfully detecting the main high frequencies which are present in the ADCP measurements within a specific range. This frequencies are the tidal and the near-inertial ones.

The near-inertial oscillations are detected and their presence is associated with active wind events. The near-inertial, tidal and steady fields that result from our study do contain dynamical information and physical meaning: the near-inertial frequencies fulfill the characteristics of the observed and modeled fields in the Catalan and Alboran sea. For the Catalan sea, the detected near-inertial period is larger than the natural inertial one. This particular feature coincides with other extensive studies in the area.

The M2 tidal fields for the Alboran sea are consistent with other studies that consider observations and/or modeling efforts. The magnitude and direction of propagation is coherent with the presence of the incoming Atlantic water. For the Catalan sea, though the tidal currents are very small, our methodology is able to predict very similar tidal situations within a specific time/space frame through two independent ADCP data sets. The differences of the predictions lie within the error bar of the ADCP observations.

The steady field has high correlations with the geostrophic field. The time-independence with which it is defined produces differences between both fields that help us to understand the dynamic content within the steady field.

Acknowledgments. The authors thank the crews of R/V 'Garcia del Cid' and R/V 'Hesperides' and all our colleagues onboard during the cruises mentioned in this paper. The cruises was funded by the Spanish National R+D Plan under projects MAR89-0550 (FE92), MAR91-0860 (PR01, PR02) and AMB95-0901 (OMEGA1, 2, 3). This paper is a contribution to the OMEGA project of the European Union Marine Science and Technology (MAST) programme (contract MAS3-CT95-0001). E.G.-G. research for this paper was financially supported by a *Generalitat de Catalunya* Doctoral Grant 'Formació de Personal Investigador'. The manuscript was finished during the postdoctoral appointment of E.G.-G. at the Jet Propulsion Laboratory/California Institute of Technology with financial assistance of the *Ministerio de Educación y Cultura* (Spain) within 'Plan de Formación de Doctores y Tecnólogos en el Extranjero'. JPL/ Caltech is under contract with the National Aeronautics and Space Administration (NASA).

REFERENCES

Alberola, C, S. Rousseau, C.Millot, M. Astraldi, J.Font, J.Garcia-Lafuente, G.P.Gasparini, A.Vangrieshim, U.Send, Tidal currents in the interior of the Western Mediterranean Sea, Oceanologica Acta. PRIMO0 special issue, 18, 2, 1995.

Allen, J.T., Subtidal and tidal currents in the vicinity of the Iceland-Faroes front, J. of Atmos. and Ocean. Tech., 12, 3, 567-588, 1995.

Candela, J., R.C. Beardsley, R. Limeburner, Removing tides from ship-mounted ADCP data, with application to the Yellow Sea, IEEE Fourth Conf. on Current Measurements, 258-266, 1990a.

Candela, J., C. Winant, A, Ruiz, Tides in the Strait of Gibraltar, J. Geophys. Res., 95, 5, 7313-7335, 1990b.

Candela, J., R.C. Beardsley, R. Limeburner, Separation of tidal and subtidal currents in ship-mounted Acoustic Doppler Current Profiler observations, J.Geophys. Res., 97, 1, 769-788, 1992.

Chereskin, T. K., M.D. Levine, A.J. Harding, L.A. Regier, Observations of Near-Inertial Waves in Acoustic Doppler Current Profier Measurements Made During the Mixed Layer Dynamics Experiment, J. Geophys. Res., 94, 6, 8135-8145, 1989.

Font, J., J. Salat, J. Tintore, Permanent features of the circulation in the Catalan Sea, Oceanol.Acta, 9, 51-57, 1988

Font, J., J. Salat, A. Julia, Marine circulation along the Ebro continental margin, Mar. Geol., 2, 445- 512, 1990.

J.Font, A. Martinez, E.Garcia-Gorriz, A. Castellon, A. Julia, M. Manriquez, A. Viudez, M.R. Vitria, Comparison of ERS-1 SAR images of the Western Mediterranean to in situ oceanographic data: PRIM-1 cruise (May 1992). Space at the service of our environment. Editor: B. Kaldeich, ESA SP-359, Noordwijk: 883-887, 1993.

Font J., E. Garcia-Ladona, E. Garcia-Gorriz, The seasonally of mesoscale motion in the Northern Current of the Western Mediterranean. Several years of evidence, Oceanologica Acta, PRIMO0 special issue, 18, 2, 1995.

Foreman, M.G., G. Freeland , A comparison of techniques for tide removal from shipmounted acoustic Doppler measurements along the southwest coast of Vancouver Island, J. Geophys. Res., 96, 9, 17007-17021, 1991.

Forsythe, G.E., M.A. Malcom, C.B.Moler, Computer Methods for Mathematical Computations, Prentice-Hall, Englewood Cliffs, N.J. (USA), 1977.

Garcia-Gorriz, E., Aplicacion de un Perfilador Acustico por Efecto Doppler a la medida de corrientes marinas en el Mediterraneo Occidental. Ph. D. Thesis. Universitat Politecnica de Catalunya, Barcelona (Spain), 1995.

Garcia-Gorriz, E., J. Font, J. Candela, Data quality control for vessel mounted Acoustic Doppler Current Profiler. Application for the Western Mediterranean Sea, Sci. Mar., 61, 4, 417-430, 1997.

Hebert, D., J. N. Moum, Decay of a Near-Inertial Wave, J.Phys. Oceanogr., 24, 2334-2351, 1994.

Heburn, W.H., P.E. LaViolette, Variations in the Structure of the Anticyclonic Gyres Found in the Albor‡n Sea, J. Geophys. Res., 95, 2, 1599-1613, 1990.

Kinder, T.H., G. Parrilla, Yes, Some of the Mediterranean Outflow Does Come From Great Depth, J. Geophys. Res., 92, 3, 2901-2906, 1987.

Kosro, P. M., Shipboard acoustic current profiling during the Coastal Dynamic Experiment. Ph.D. Thesis, Univ. of California at San Diego.

Lozano C.J., J. Candela, The M2 tide in the Mediterranean Sea: Dynamical analysis and data assimilation, Oceanologica Acta, 18, 4, 419- 441, 1994

Lwiza, K.M.M., D.G. Bowers, J.H. Simpson, Residual and tidal flow at a tidal mixing front in the North sea, Cont. Shelf Res., 11, 11, 1379-1395, 1991.

Millot C, M.Crepon, Inertial oscillations on the continental shelf of the Gulf of Lions-Observations and theory, J. Phys. Oceanogr., 11, 639-657, 1981.

Millot C., Circulation in the Western Mediterranean Sea, Oceanologica Acta, 10, 2, 143-149, 1987.

Munchow A., R.W. Garvine, T.F. Pfeiffer, Subtidal currents from a shipboard acoustic Doppler current profiler in tidally dominated waters, Cont. Shelf Res., 12, 4, 499-515, 1992.

Pollard R.T, R.C.Millard, Comparison between observed an simulated wind-generated inertial oscillations, Deep-Sea Res, 17, 813-821, 1970.

Prunet, P., J.F. Minster, D. Ruiz-Pino, I. Dadou, Assimilation of surface data in a one-dimensional physical-biogeochemical model of the surface ocean. 1. Method and preliminary results, Global Biogeochem. Cycles, 10, 1, 111-138, 1996.

Salat J., J.Tintore, J. Font, D.P. Wang, M. Vieira, Near-Inertial Motion on the Shelf-Slope Front off Northeast Spain, J. Geophys. Res., 97, 5, 7277-7281, 1992.

Tintore, J., D.P. Wang, E. Garcia, A. Viudez, Near-inertial motions in the coastal ocean, Journal of Marine Systems, 6, 301-312, 1995.

Thomson, R.E., P.H. LeBlond, A.B. Rabinovich, Satellite-tracked drifter measurement of inertial and semidiurnal currents in the northeast Pacific, J. Geophys. Res., 103, 1, 1039-1052, 1998.

Tsimplis, M.N., R. Proctor, R.A. Flather, A two-dimensional tidal model for the Mediterranean Sea, J. Geophys. Res., 100 , 8, 16223-16239, 1995.

Viudez, A., Forzamiento de flujos ageostroficos. Mar de Alboran y plataforma de Mallorca-Cabrera, Ph. D. Thesis, Universitat de les Illes Balears (Palma de Mallorca, Spain), 1994.

FIGURE CAPTIONS

Figure 1:

a) Location of the Alboran basin in the Western Mediterranean sea. Isobaths of 0, 1000 and 2000 m are plotted.

b) The locations of the 1-hour-averaged ADCP profiles during FE92 cruise are marked with consecutive circles, which linked by a dashed line. The OMEGA1-2-3 10-minute-average locations are linked by the solid line. The two stars indicate the coordinates for the initial time of the cruises.

c) The diamonds locate the 30-minute-averaged ADCP profile positions of PR01-2 cruises. The star indicates the location for initial time of the cruises.

Figure 2: The fraction of explained variance R within the period interval 11 to 25 h for the cruises FE92 (a), PR01 (b), PR02 (c), OMEGA1 (d), OMEGA2 (e), and OMEGA3 (f). The vertical scales of this 6 plots in are not equal in order to enhance the visual effect of the peaks in the curve of R. PR01 (b) and PR02 (c) plots have a square in the point (12.4,0.2) and three stars are located (12.42, 0.35) for the OMEGA1 (d), 2 (e) and 3 (f) plots to facilitate a visual reference of the differences between them. The solid vertical line in each plot labels the natural inertial period corresponding the cruise mean latitude

Figure 3: F-test quotient results for the cruise PR02. Three different near-inertial periods: 19.8 (a), 20.0 (b) and 20.2 h (c) are considered in the F-test quotient computation.

Figure 4:

a) Phase of the FE92 near-inertial oscillations with depth related to 16 m.

b) Evolution of the phase and amplitude values for a location in PR02 domain. Each one of the polar plots displays consecutive progressive times. This single near-inertial oscillation of approximately 10.4 cm/s is quasi-circular and clockwise.

Figure 5: The u component of the near-inertial current resulting from the model by Pollard and Millard (1970) corresponds to the solid lines. The model is forced by ERS-1 winds for the time of the FE92 cruise. Three different decay coefficients are considered, 4 (a), 8 (b) and 20 days (c). The dashed lines display the near-inertial u component filtered out from the FE92 ADCP observations.

Figure 6: The M2 tidal ellipse orientations resulting from the FE92 ADCP observations.

Figure 7: The M2 tidal ellipse orientations for the PR01 (a) and PR02 cruises(b). Contoured surface elevation tidal amplitudes for PR01 (c) and PR02 (d).

Figure 8: 1 h averaged ADCP current velocities (a), the fitted field considering both the M2 tide and near-inertial period of 19.1 h (b), the steady field (c), and the residual field (d) for the FE92 cruise at 24 m deep.

Figure 9: Geostrophic field at 24 m for FE92 (a), PR01 (b), and PR02 (c).

Figure 10: ADCP observations (a), the fitted field considering the M2 tide and near-inertial period of 20 h (b), the steady field (c), and the residual field (d) for PR01 at depth 24 m. Same for PR02 at 24 m (e, f, g and h respectively).

Figure 11: ERS-1 wind stress and corresponding error bars for the FE92 (a) and PR01 and 2 cruises (b). NSCAT wind stress for the cruises OMEGA1, 2 and 3 (c).

Figure 12:

a) Detection of periodical signals with random data as input and holding the same temporal and spatial coordinates as in FE92.
b) Detection of periodical signals with a pure M2 tide signal as input at the actual time and spatial locations as in OMEGA1.

c) Detection of periodical signals based on the Complex Demodulation formulation by Hebert and Moum (1994) for PR01 observations.

d) Same as c) but for OMEGA2 observations.

Figure 13: Detection of periodical signals within the interval 25 to 130 h for the FE92 cruise.

Figure 14: Geostrophic field computed from CTD casts minus the time-independent steady component from ADCP observations at 24 m for the PR01 (a) and PR02 (b) cruises.

Figure 15: Current field resulting from adding the steady plus the residual component at 24 m for FE92 (a), PR01 (b), and PR02 (c) cruises.

TABLES

Table 1: Periods corresponding to peaks of R in Fig. 2

Cruise	Location	11 to 14h	14 to 18h	18 to 25h
FE92	Alboran sea	12.4	15.1	19.1
PR01	Catalan sea	12.5	16.5	20.8
PR02	Catalan sea	12.2	14.1	19.9
OMEGA1	Alboran sea	12.6	15.5	20.0* Not prominent
OMEGA2	Alboran sea	11.9	16.3	20.1
OMEGA3	Alboran sea	12.6	16.4	21.7* Not prominent

Table 2: Percent of energy associated with the first three EOF modes of the steady and geostrophic fields for cruises FE92 and PR01.

Cruise	Field	Mode 1	Mode 2	Mode 3
FE92	Steady	69.27	18.69	6.40
FE92	Geostrophic	81.42	12.40	2.84
PR01	Steady	96.58	2.82	0.23
PR01	Geostrophic	96.59	3.20	0.14

FIGURE 1.

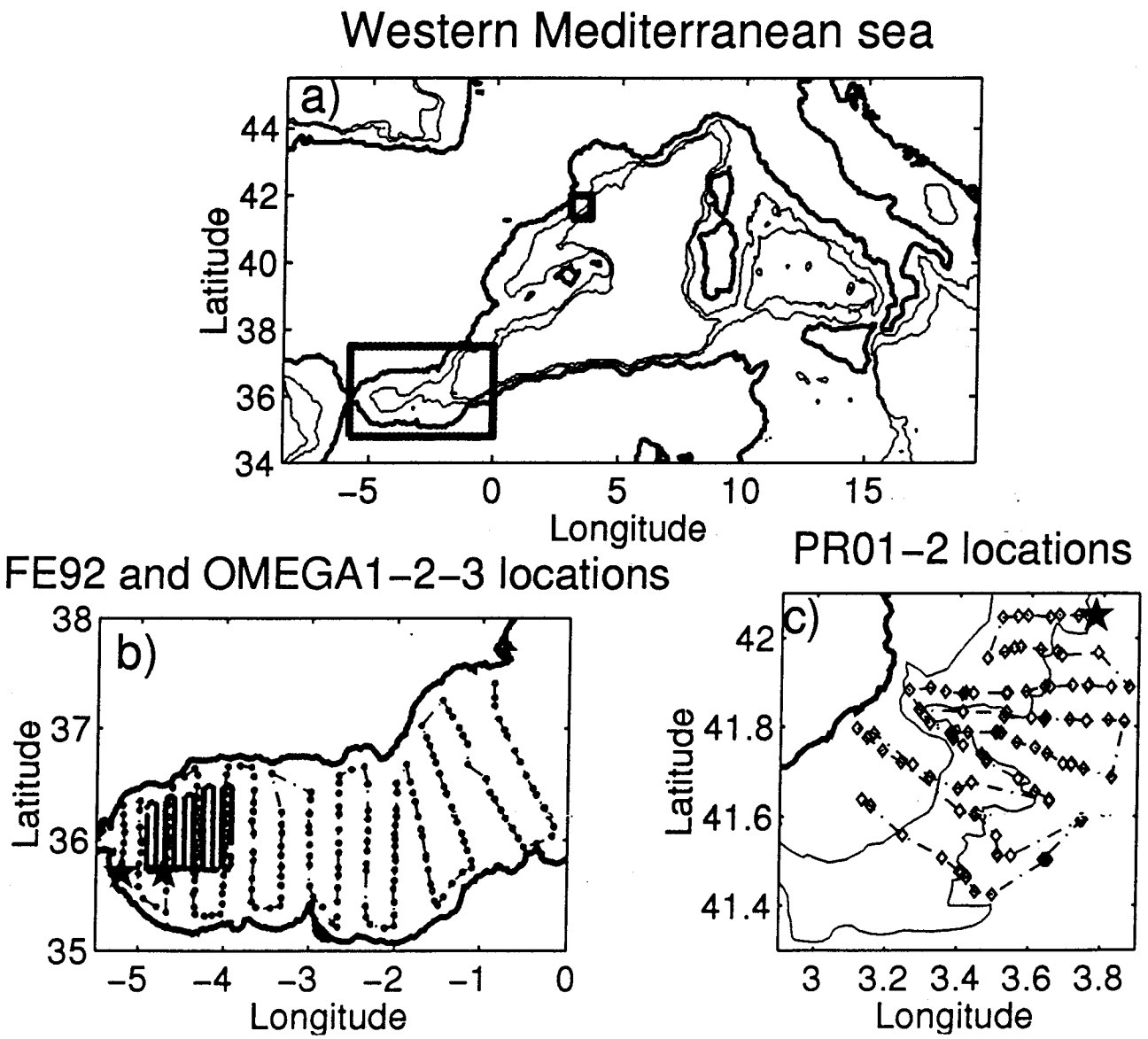
Western Mediterranean sea
a)
Latitude
Longitude
44
42
40
38
36
34
-5
0
5
10
15
FE92 and OMEGA1-2-3 locations
b)
Latitude
Longitude
38
37
36
35
-5
-4
-3
-2
-1
0
PR01-2 locations
c)
Latitude
Longitude
42
41.8
41.6
41.4
3
3.2
3.4
3.6
3.8

FIGURE 2

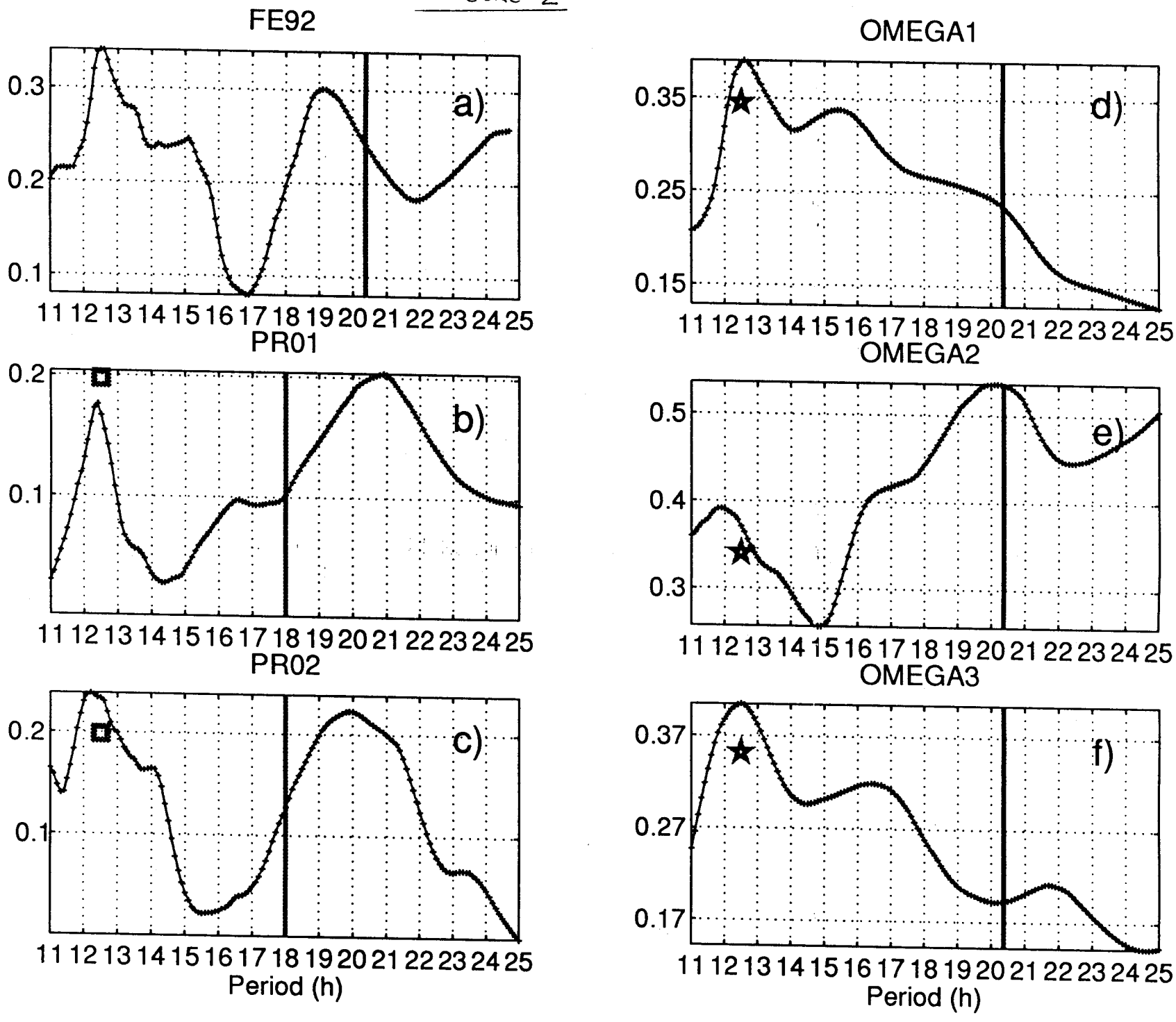
FE92
a)
0.3
0.2
0.1
11 12 13 14 15 16 17 18 19 20 21 22 23 24 25
PR01
b)
0.2
0.1
11 12 13 14 15 16 17 18 19 20 21 22 23 24 25
PR02
c)
0.2
0.1
11 12 13 14 15 16 17 18 19 20 21 22 23 24 25
Period (h)
OMEGA1
d)
0.35
0.25
0.15
11 12 13 14 15 16 17 18 19 20 21 22 23 24 25
OMEGA2
e)
0.5
0.4
0.3
11 12 13 14 15 16 17 18 19 20 21 22 23 24 25
OMEGA3
f)
0.37
0.27
0.17
11 12 13 14 15 16 17 18 19 20 21 22 23 24 25
Period (h)

FIGURE 3

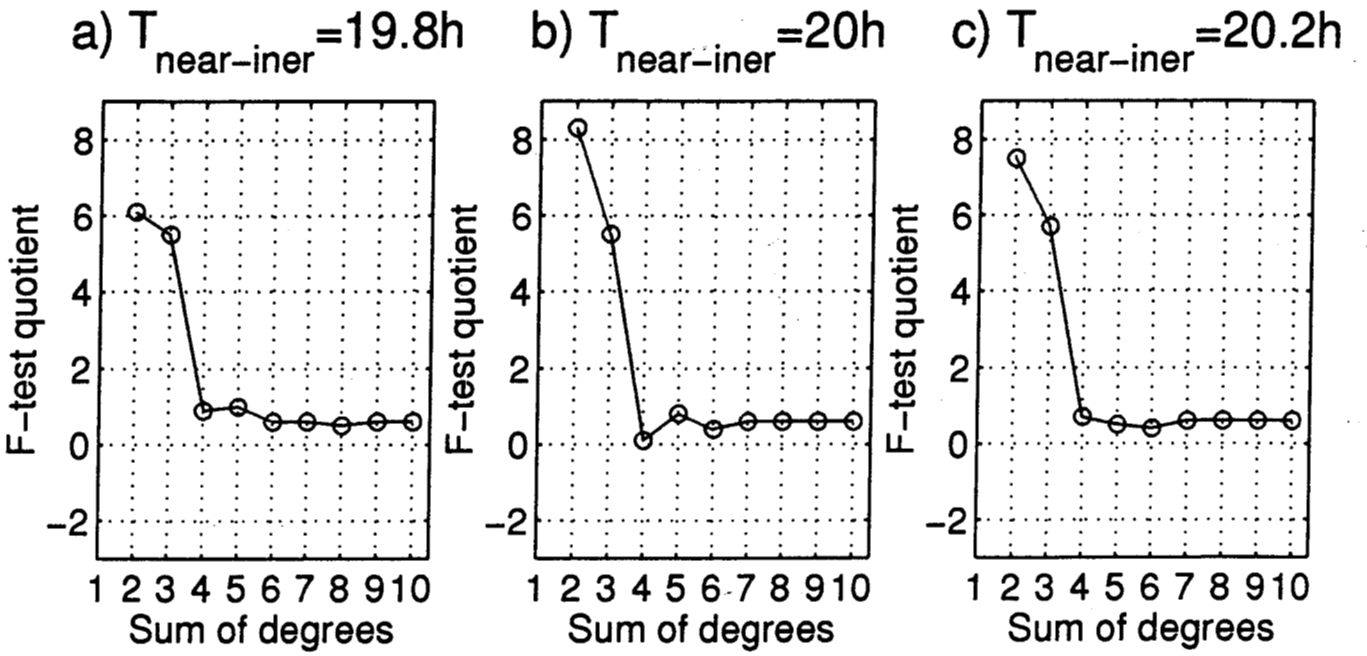
a) T near−iner =19.8h
b) T near−iner =20h
c) T near−iner =20.2h
F−test quotient
8
6
4
2
0
−2
1 2 3 4 5 6 7 8 9 10
Sum of degrees

FIGURE 4

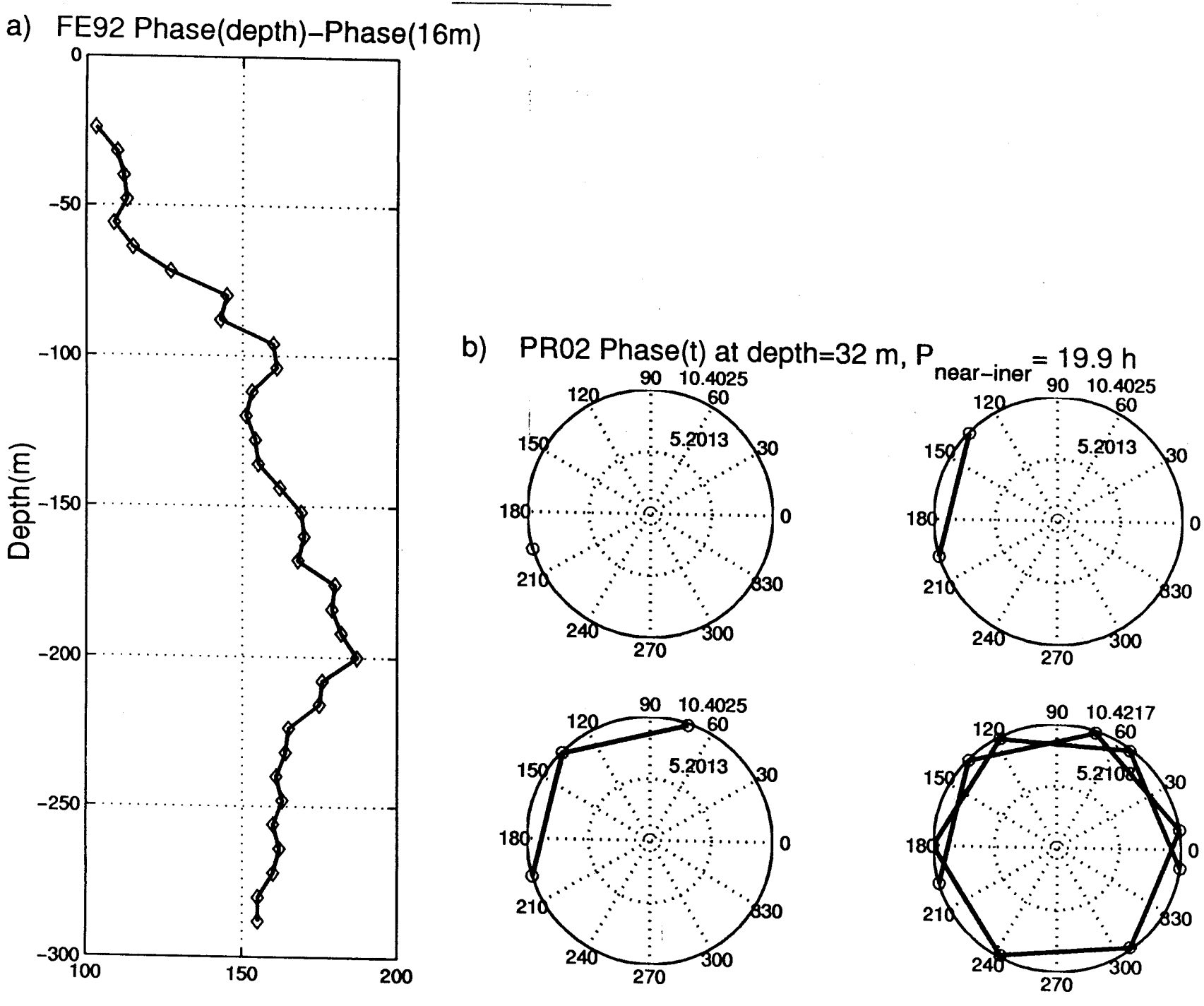
a) FE92 Phase(depth)–Phase(16m)
Depth(m)
0
-50
-100
-150
-200
-250
-300
100
150
200
b) PR02 Phase(t) at depth=32 m, P near-iner = 19.9 h
90
10.4025
60
30
0
330
300
270
240
210
180
150
120
5.2013
10.4217
5.2108

FIGURE 5

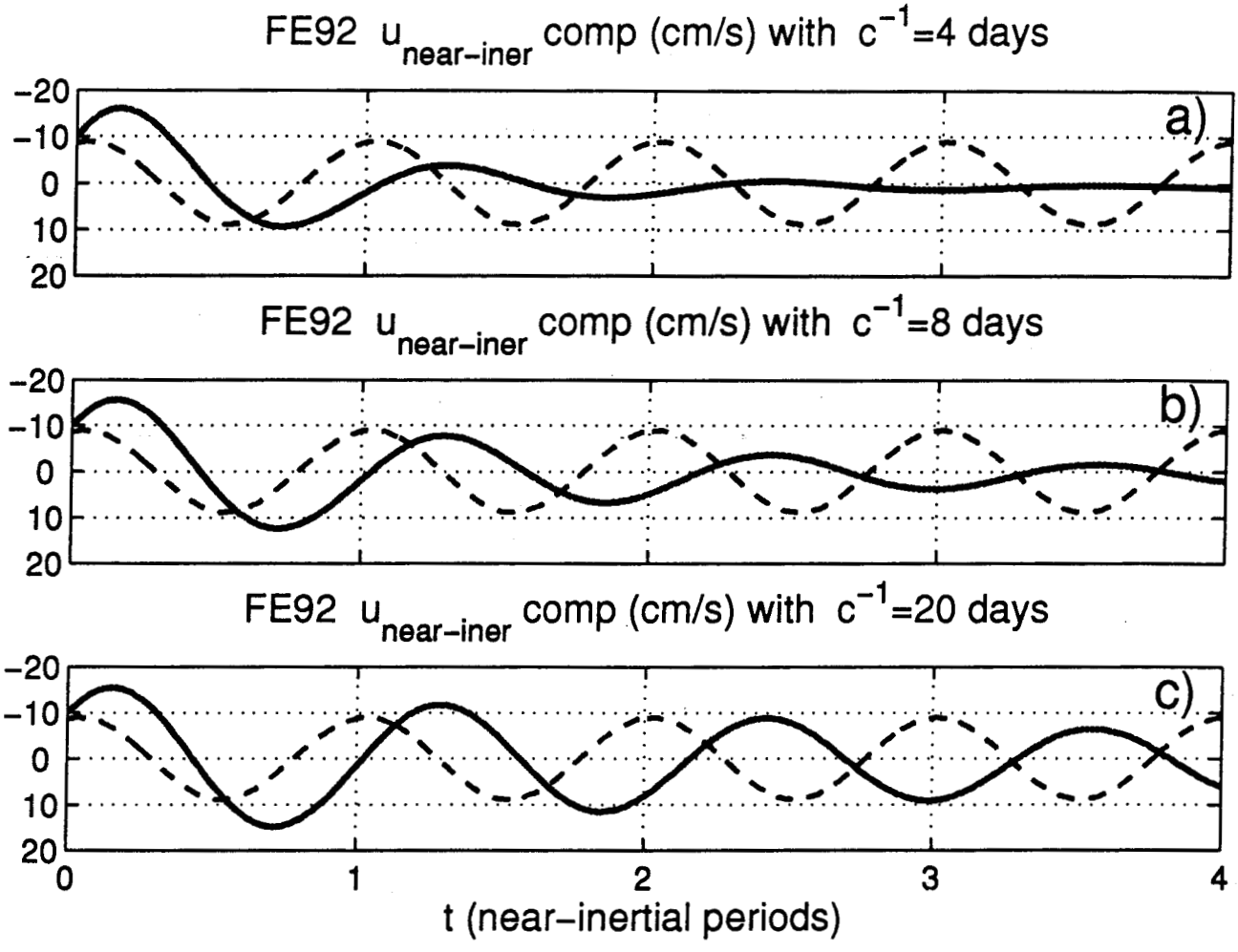
FE92 u near-iner comp (cm/s) with c^-1=4 days
a)
FE92 u near-iner comp (cm/s) with c^-1=8 days
b)
FE92 u near-iner comp (cm/s) with c^-1=20 days
c)
−20
−10
0
10
20
0
1
2
3
4
t (near−inertial periods)

FIGURE 6

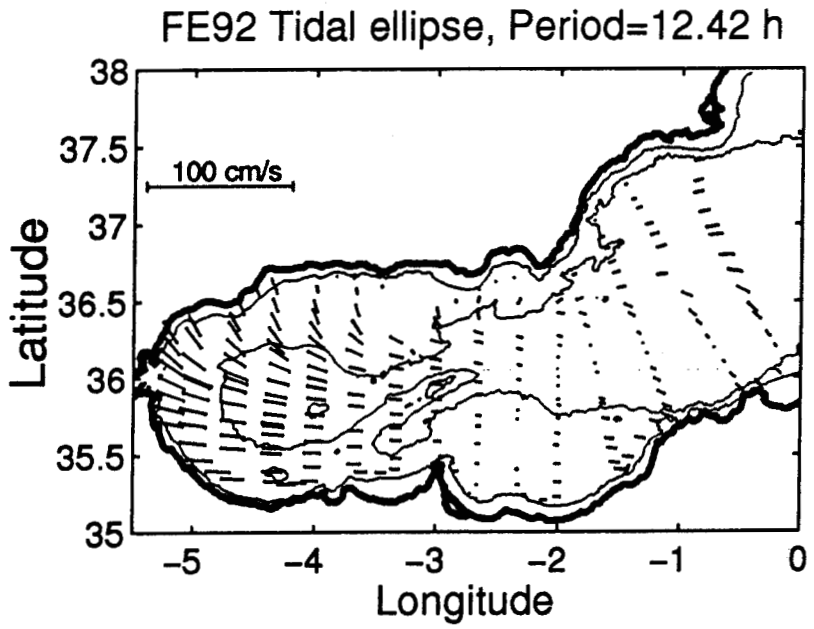
FE92 Tidal ellipse, Period=12.42 h
100 cm/s
Latitude
Longitude
38
37.5
37
36.5
36
35.5
35
-5
-4
-3
-2
-1
0

FIGURE 7

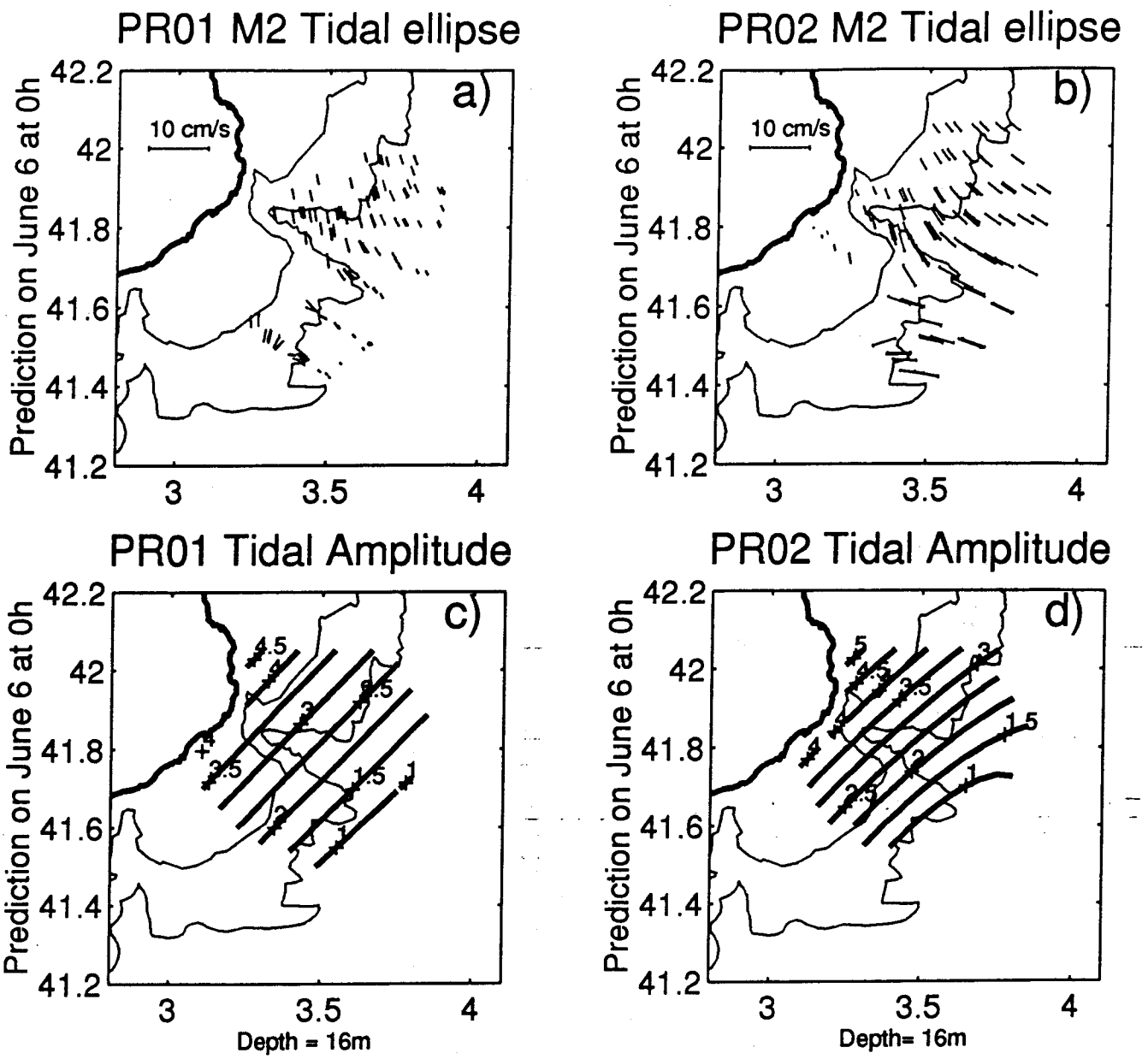
PR01 M2 Tidal ellipse
PR02 M2 Tidal ellipse
PR01 Tidal Amplitude
PR02 Tidal Amplitude
a)
b)
c)
d)
10 cm/s
Prediction on June 6 at 0h
42.2
42
41.8
41.6
41.4
41.2
3
3.5
4
Depth = 16m
Depth= 16m

FIGURE 8

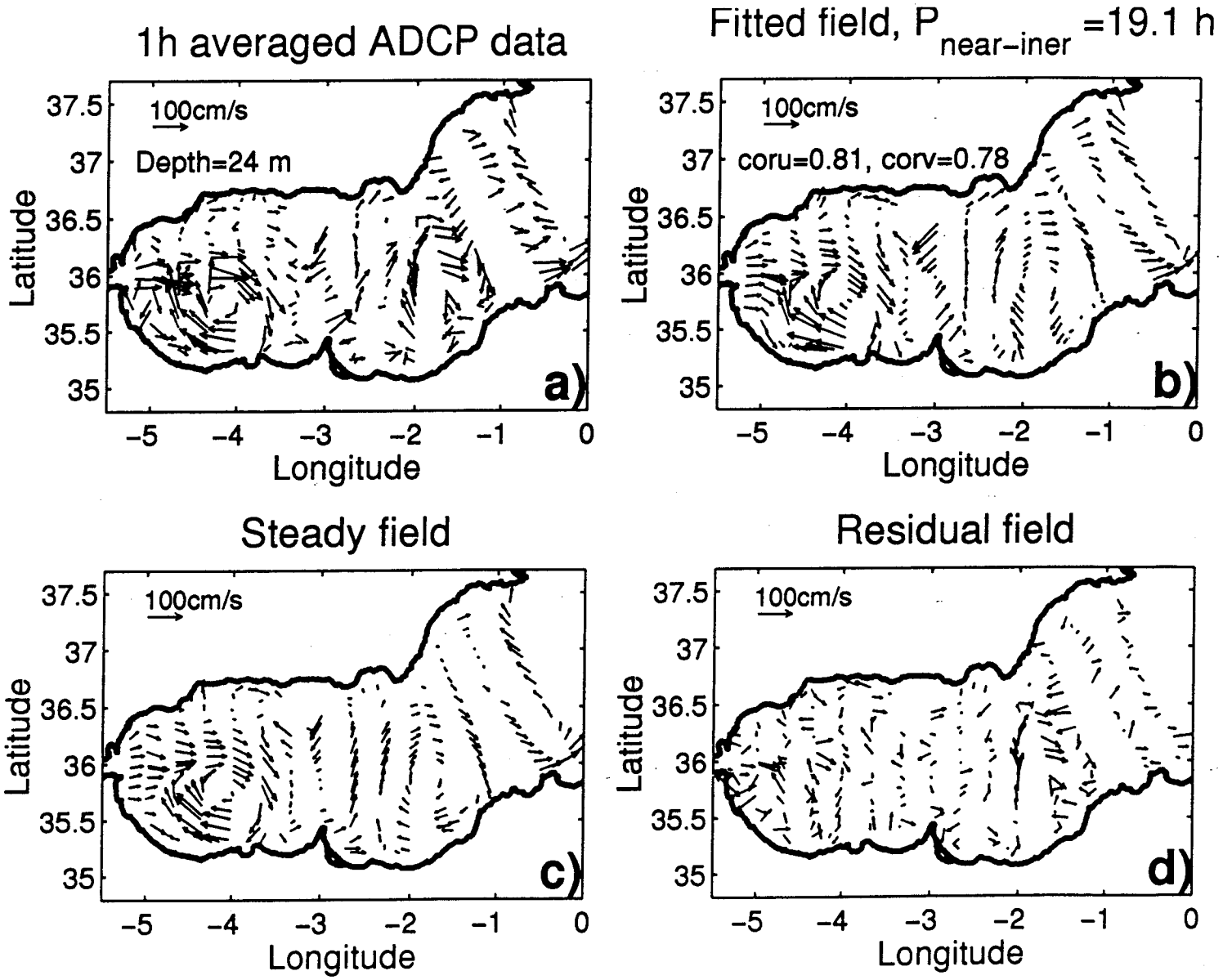
1h averaged ADCP data
Fitted field, P near-iner =19.1 h
100cm/s
Depth=24 m
coru=0.81, corv=0.78
Steady field
Residual field
Latitude
Longitude
37.5
37
36.5
36
35.5
35
-5
-4
-3
-2
-1
0
a)
b)
c)
d)

FIGURE 9

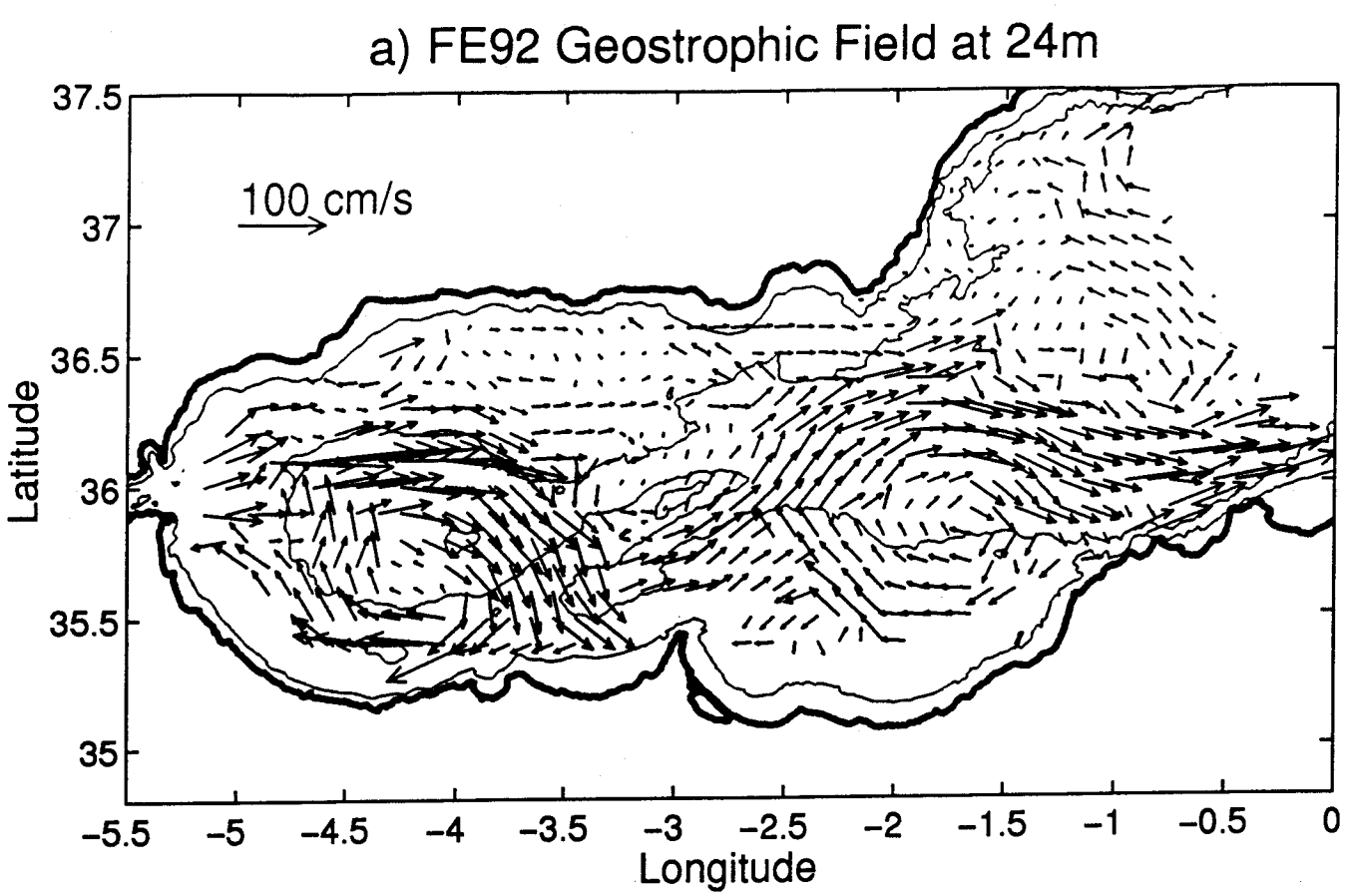
a) FE92 Geostrophic Field at 24m
100 cm/s
37.5
37
36.5
36
35.5
35
Latitude
-5.5
-5
-4.5
-4
-3.5
-3
-2.5
-2
-1.5
-1
-0.5
0
Longitude

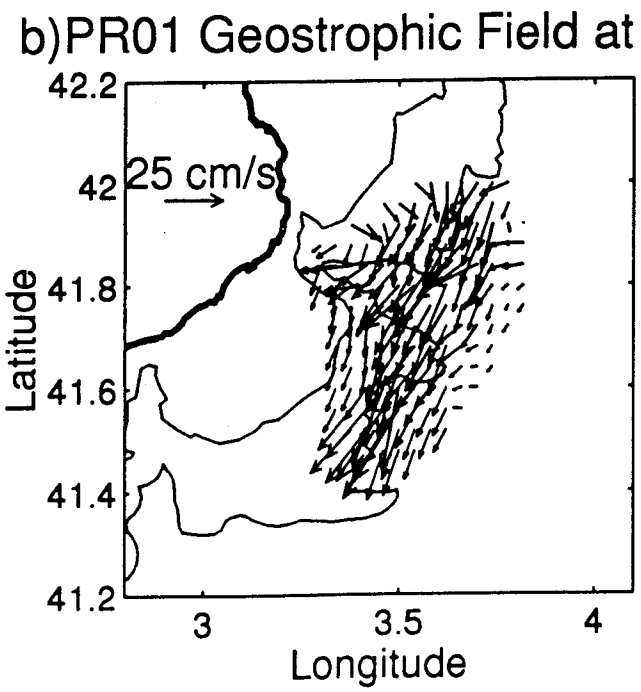
b)PR01 Geostrophic Field at 24m
25 cm/s
42.2
42
41.8
41.6
41.4
41.2
Latitude
3
3.5
4
Longitude

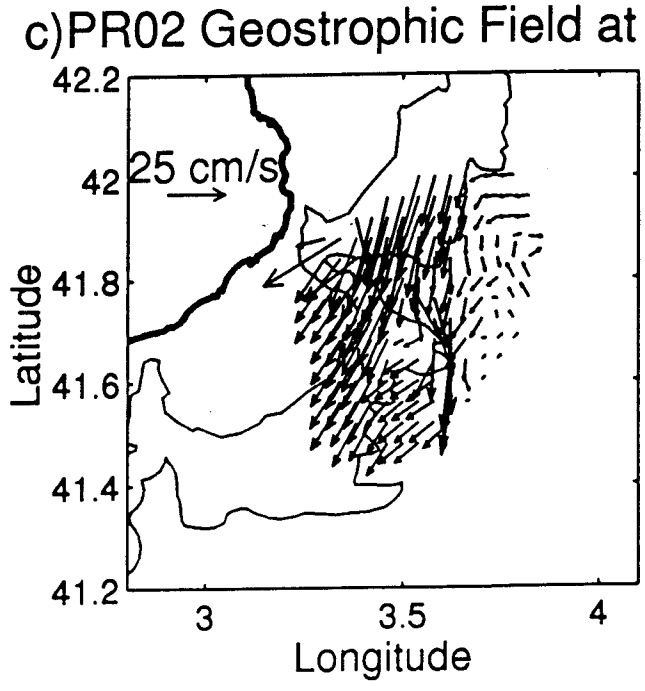
c)PR02 Geostrophic Field at 24m
25 cm/s
42.2
42
41.8
41.6
41.4
41.2
Latitude
3
3.5
4
Longitude

FIGURE 10

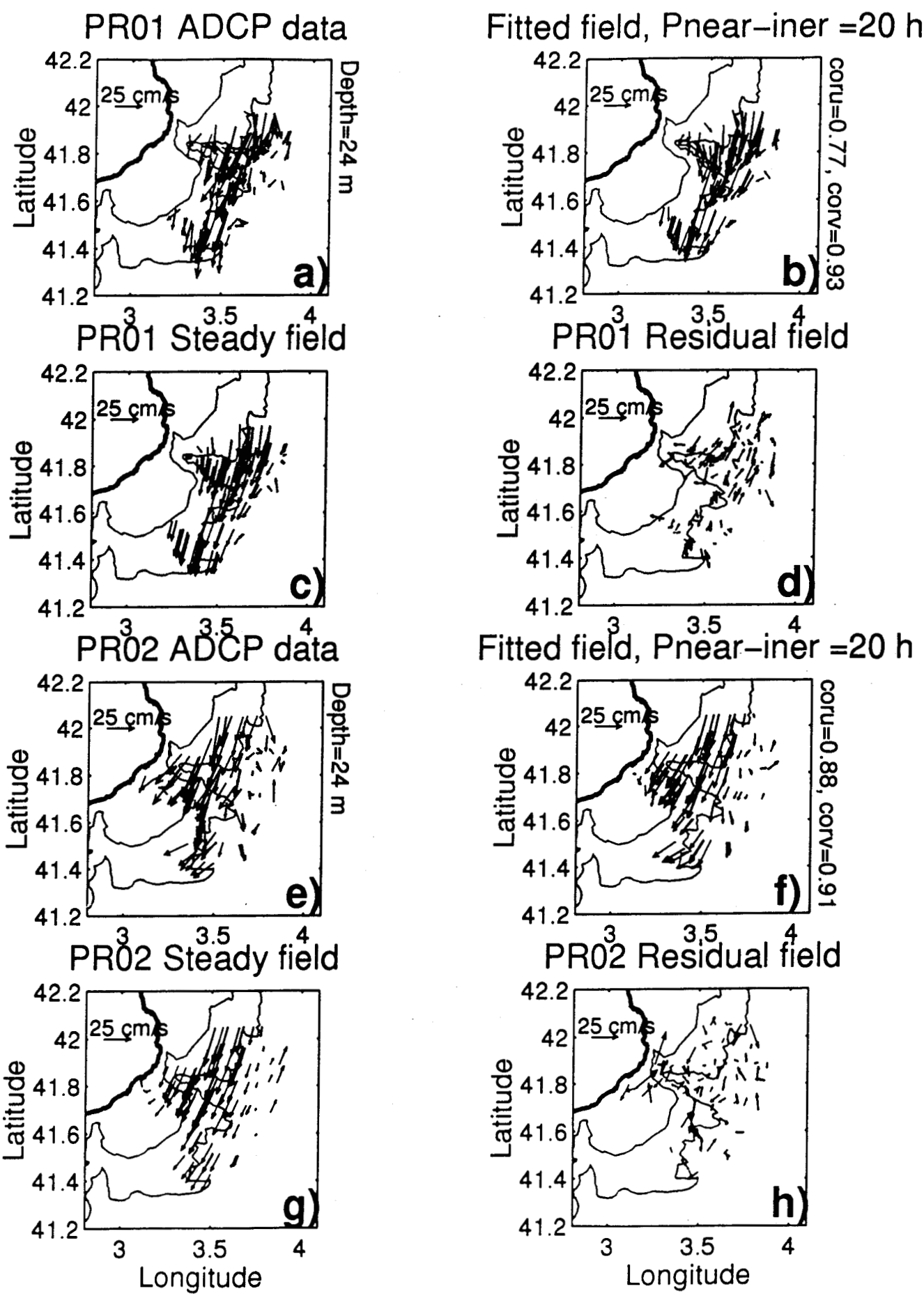
PR01 ADCP data
Fitted field, Pnear–iner =20 h
PR01 Steady field
PR01 Residual field
PR02 ADCP data
Fitted field, Pnear–iner =20 h
PR02 Steady field
PR02 Residual field
25 cm/s
Depth=24 m
coru=0.77, corv=0.93
coru=0.88, corv=0.91
a)
b)
c)
d)
e)
f)
g)
h)
Latitude
Longitude
42.2
42
41.8
41.6
41.4
41.2
3
3.5
4

FIGURE 11

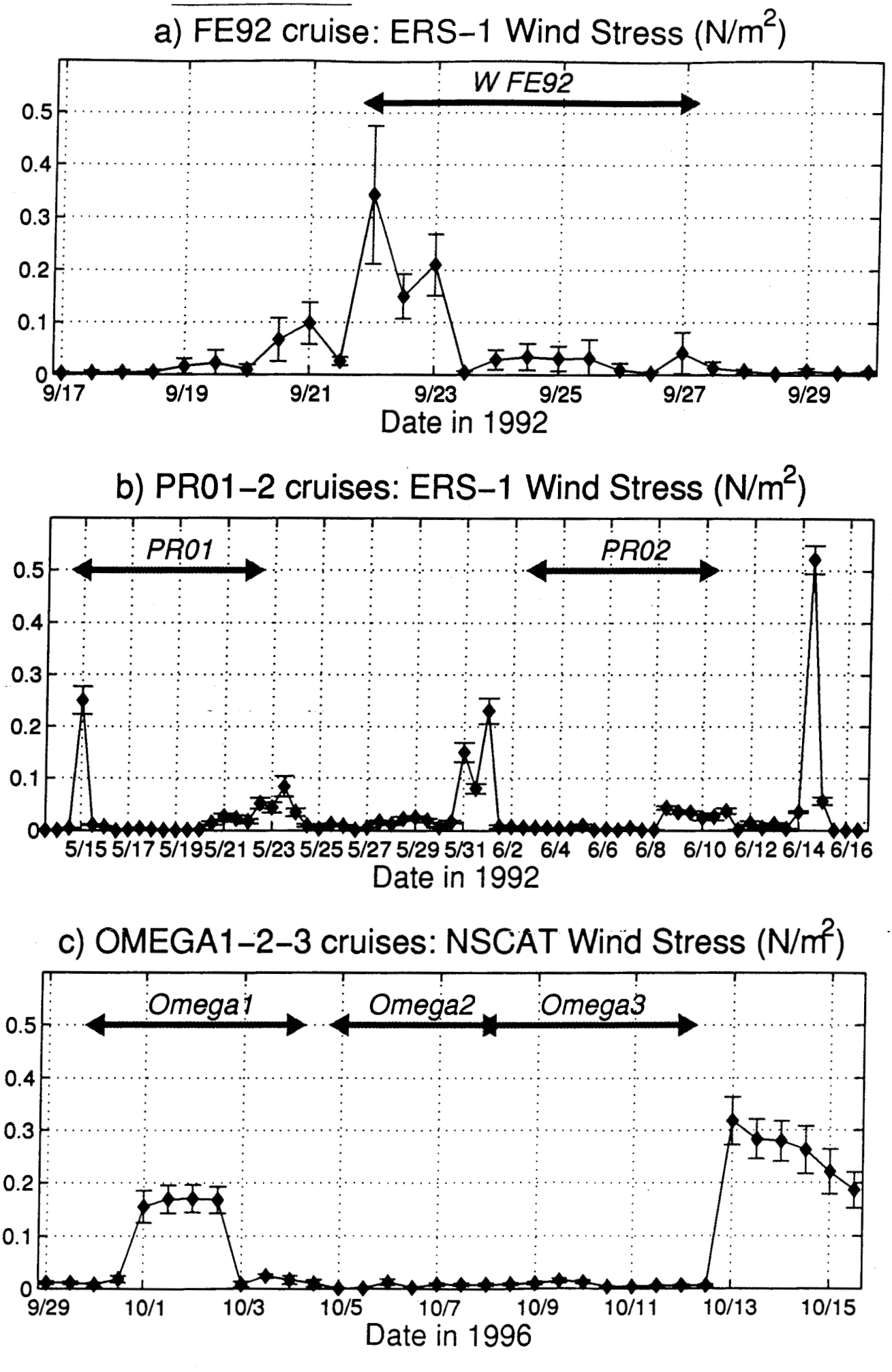
a) FE92 cruise: ERS-1 Wind Stress (N/m2)
W FE92
0.5
0.4
0.3
0.2
0.1
0
9/17
9/19
9/21
9/23
9/25
9/27
9/29
Date in 1992
b) PR01-2 cruises: ERS-1 Wind Stress (N/m2)
PR01
PR02
0.5
0.4
0.3
0.2
0.1
0
5/15 5/17 5/19 5/21 5/23 5/25 5/27 5/29 5/31 6/2 6/4 6/6 6/8 6/10 6/12 6/14 6/16
Date in 1992
c) OMEGA1-2-3 cruises: NSCAT Wind Stress (N/m2)
Omega1
Omega2
Omega3
0.5
0.4
0.3
0.2
0.1
0
9/29
10/1
10/3
10/5
10/7
10/9
10/11
10/13
10/15
Date in 1996

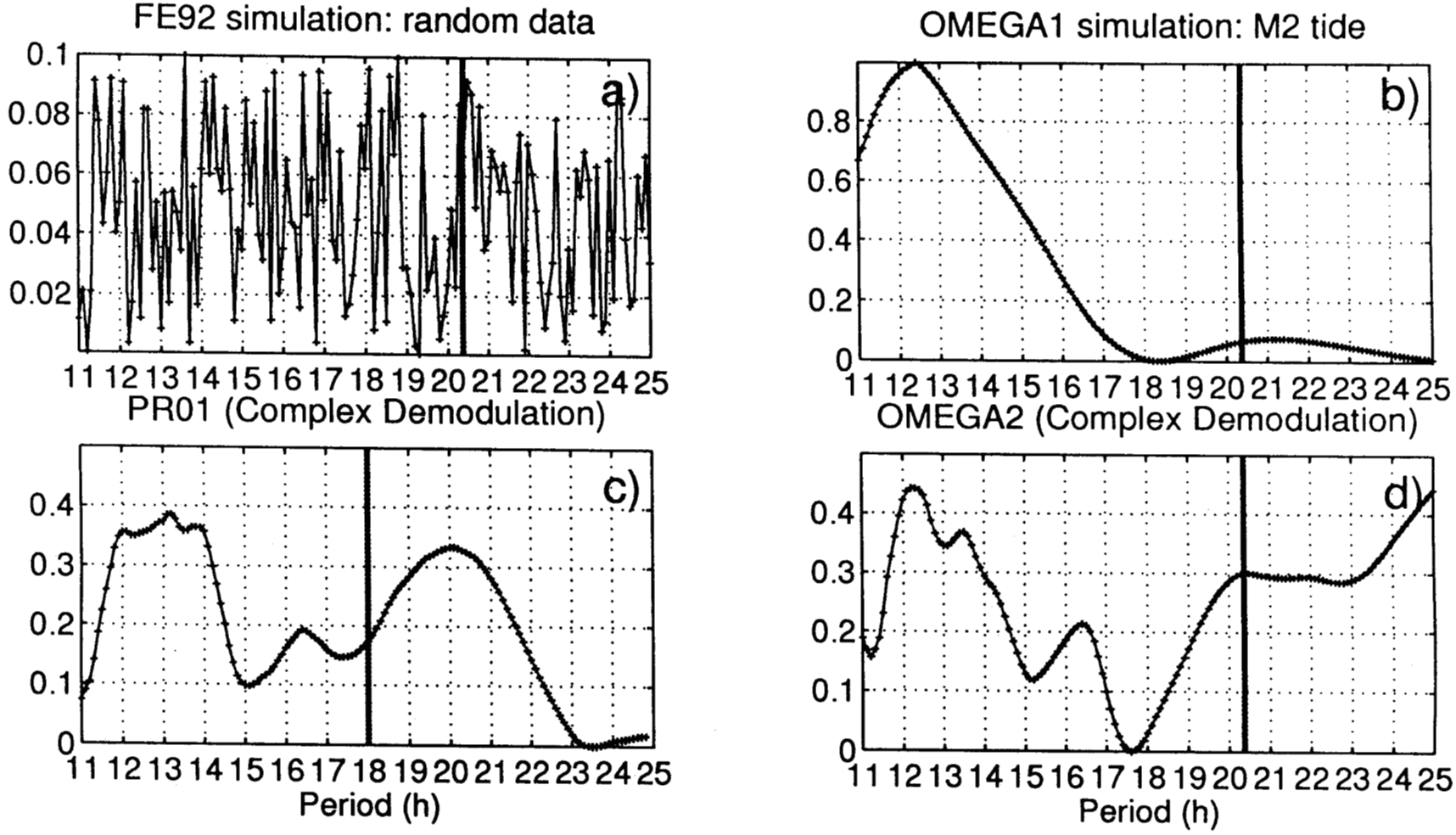
FE92 simulation: random data
a)
0.1
0.08
0.06
0.04
0.02
11 12 13 14 15 16 17 18 19 20 21 22 23 24 25
PR01 (Complex Demodulation)
OMEGA1 simulation: M2 tide
b)
0.8
0.6
0.4
0.2
0
11 12 13 14 15 16 17 18 19 20 21 22 23 24 25
OMEGA2 (Complex Demodulation)
c)
0.4
0.3
0.2
0.1
0
11 12 13 14 15 16 17 18 19 20 21 22 23 24 25
Period (h)
d)
0.4
0.3
0.2
0.1
0
11 12 13 14 15 16 17 18 19 20 21 22 23 24 25
Period (h)

FIGURE 12

FIGURE 13

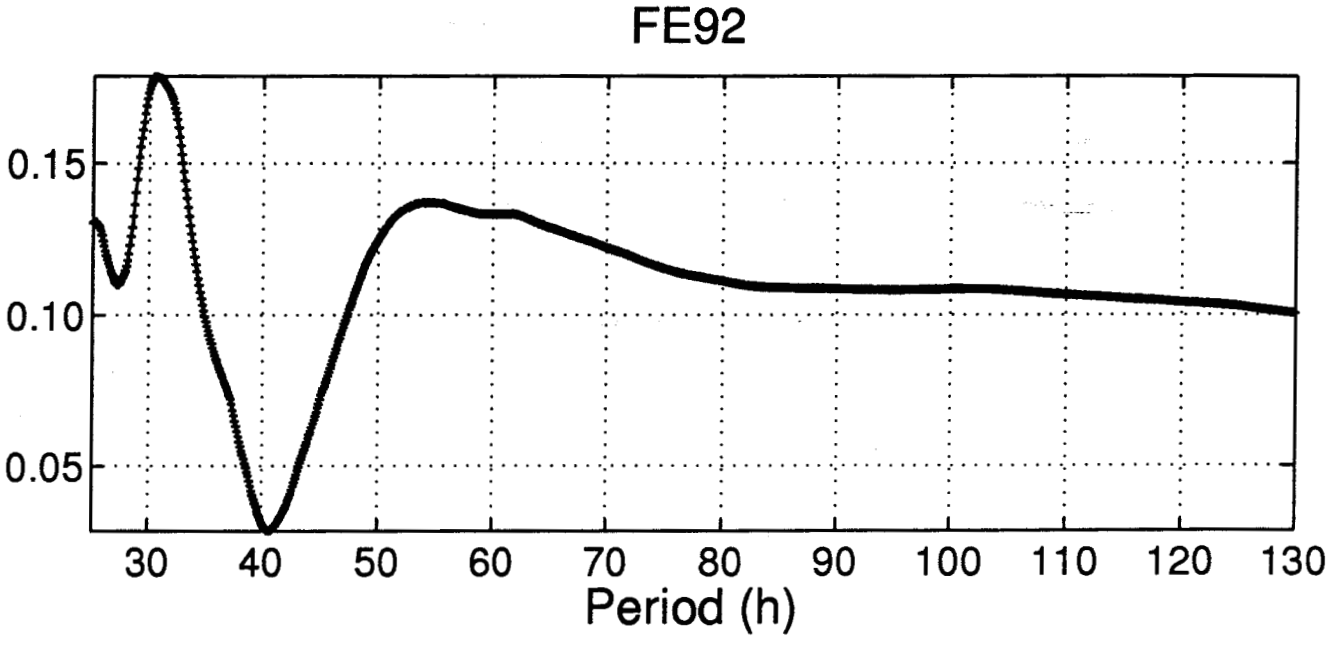

FIGURE 14

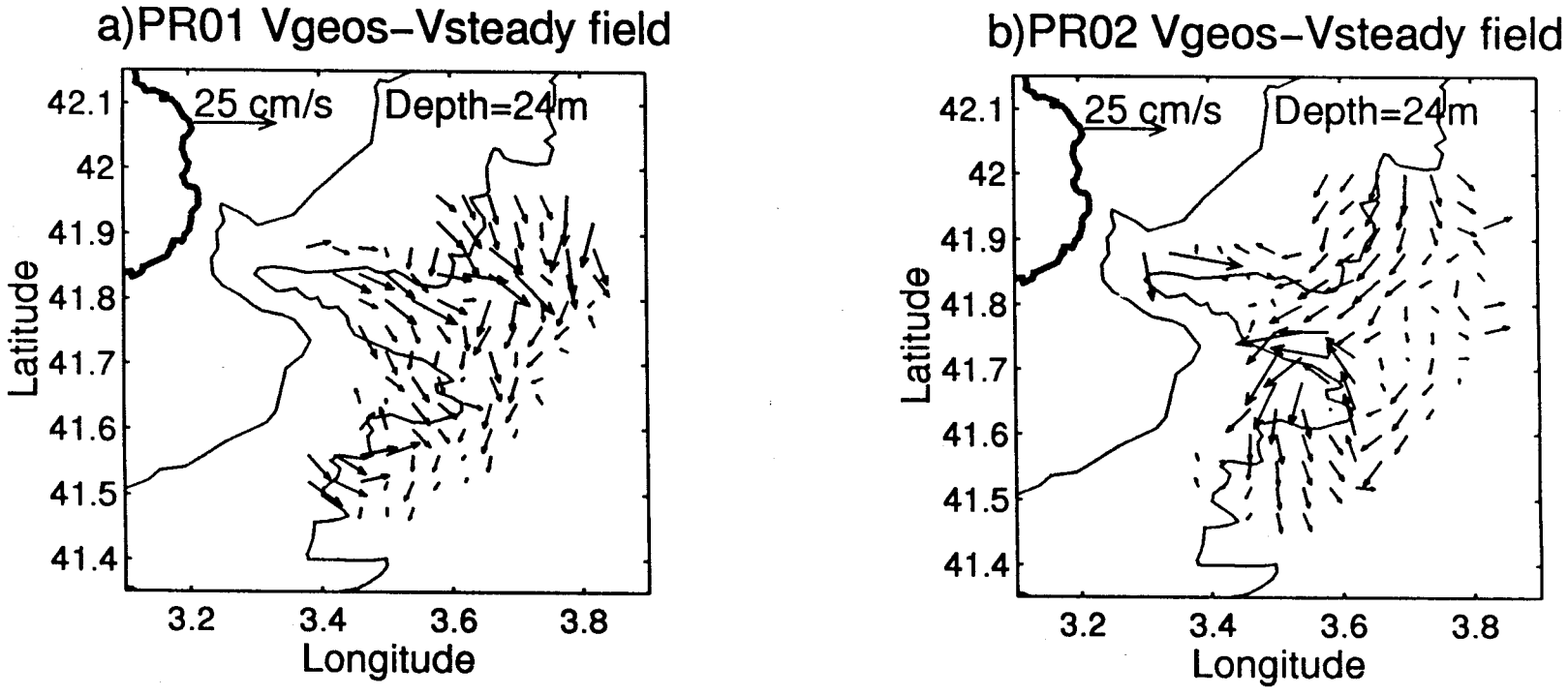
a)PR01 Vgeos–Vsteady field
25 cm/s
Depth=24m
42.1
42
41.9
41.8
41.7
41.6
41.5
41.4
Latitude
3.2
3.4
3.6
3.8
Longitude
b)PR02 Vgeos–Vsteady field
25 cm/s
Depth=24m
42.1
42
41.9
41.8
41.7
41.6
41.5
41.4
Latitude
3.2
3.4
3.6
3.8
Longitude

FIGURE 15

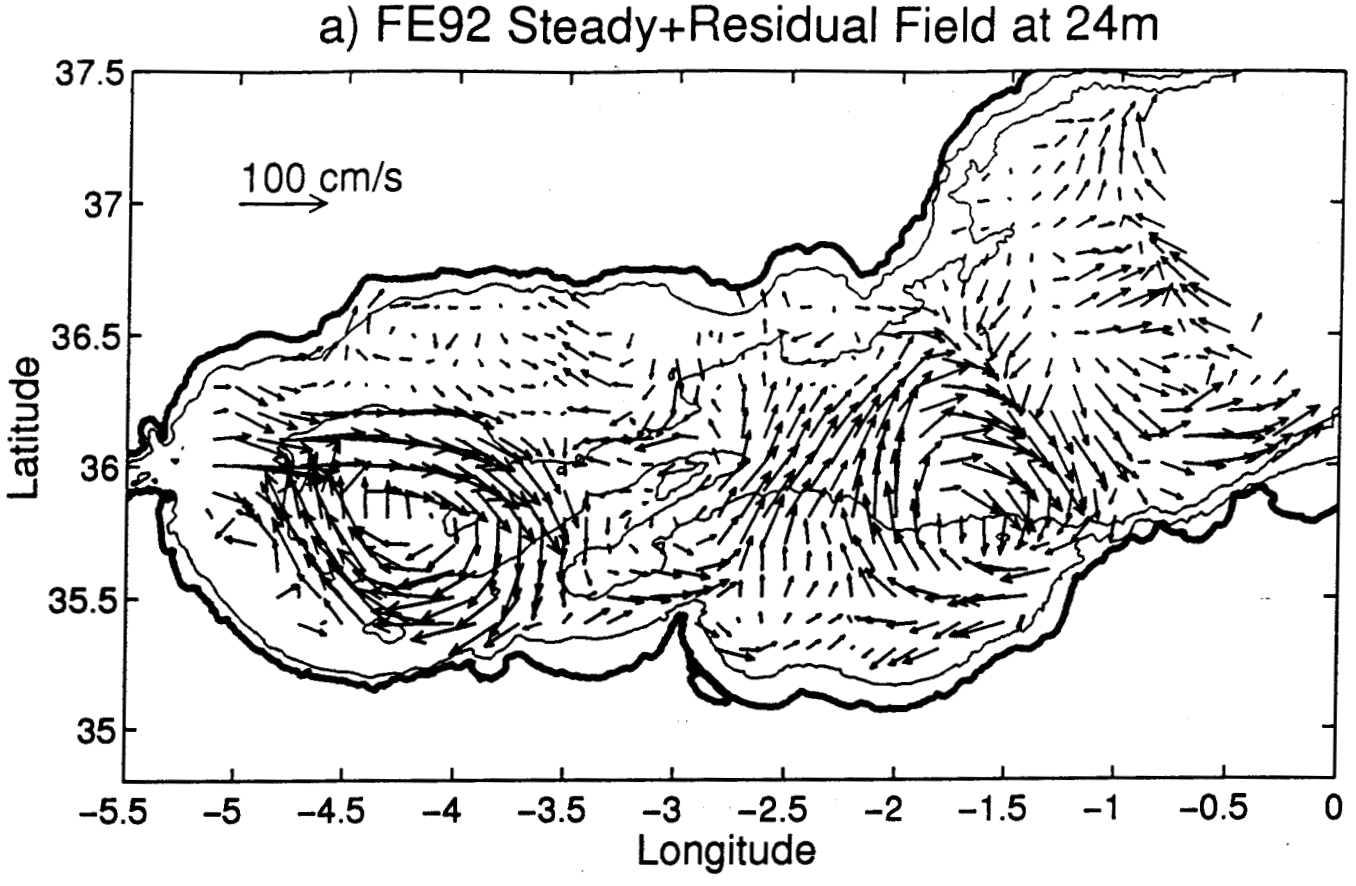
a) FE92 Steady+Residual Field at 24m
100 cm/s
37.5
37
36.5
36
35.5
35
Latitude
-5.5
-5
-4.5
-4
-3.5
-3
-2.5
-2
-1.5
-1
-0.5
0
Longitude

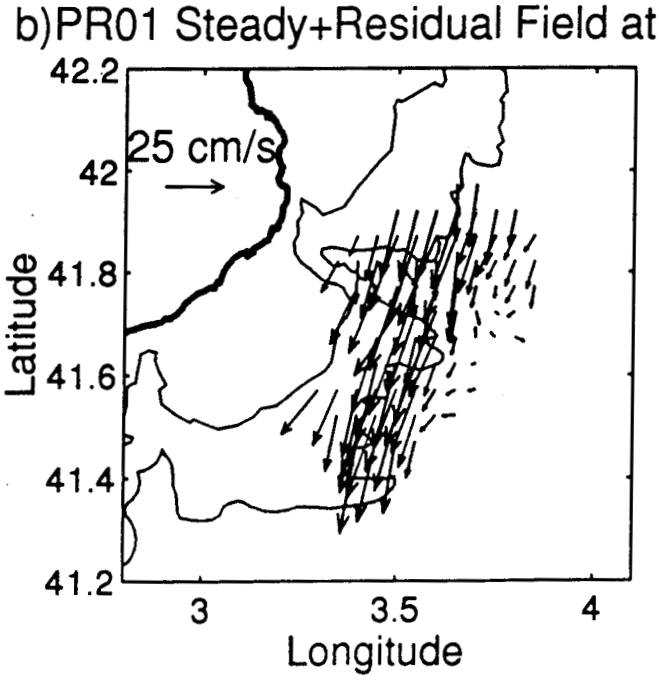
b)PR01 Steady+Residual Field at 24m
25 cm/s
42.2
42
41.8
41.6
41.4
41.2
Latitude
3
3.5
4
Longitude

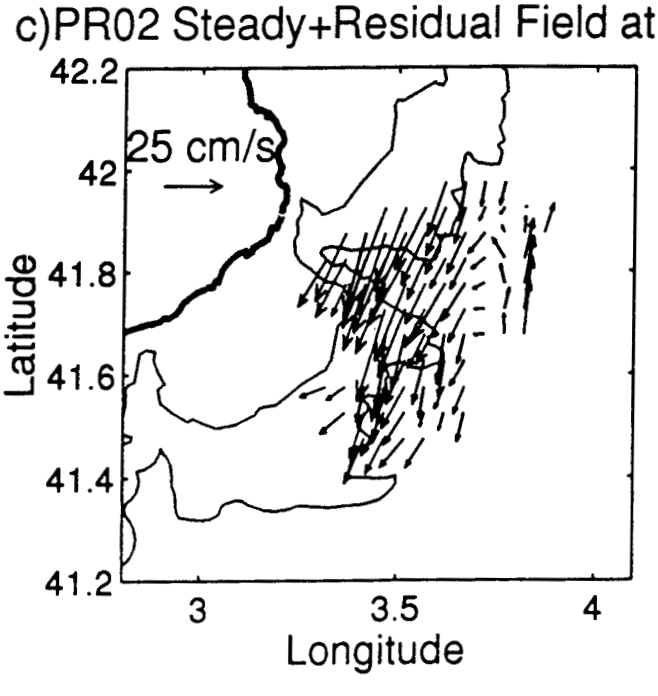
c)PR02 Steady+Residual Field at 24m
25 cm/s
42.2
42
41.8
41.6
41.4
41.2
Latitude
3
3.5
4
Longitude